Warm pool ocean heat content regulates ocean-continent moisture transport

3 Zhimin Jian^{1,*}, Yue Wang^{1,*}, Haowen Dang^{1,*}, Mahyar Mohtadi², Yair Rosenthal³, David W.

4 Lea⁴, Zhongfang Liu¹, Haiyan Jin¹, Liming Ye⁵, Wolfgang Kuhnt⁶, Xingxing Wang¹

6 ¹State Key Laboratory of Marine Geology, Tongji University, Shanghai 200092, China. ²MARUM-Center for

7 Marine Environmental Sciences, University of Bremen, 28359 Bremen, Germany. ³Department of Marine and

Coastal Science and Department of Earth and Planetary Sciences, Rutgers University, New Brunswick, NJ 08901,

USA. ⁴Department of Earth Science, University of California, Santa Barbara, CA 93106, USA. ⁵Second Institute

of Oceanography, Ministry of Natural Resource, Hangzhou 310012, China. ⁶Institute of Geosciences, Christian-

Albrechts-University, D-24118 Kiel, Germany.

* Correspondence and requests for materials should be addressed to Z.J. (jian@tongji.edu.cn), Y.W.

14 (163wangyue@163.com) or H.D. (hwdang@tongji.edu.cn)

The Indo-Pacific Warm Pool (IPWP) exerts a dominant role on global climate by releasing huge amounts of water vapor and latent heat to the atmosphere and modulating upper ocean heat content (OHC), which has been implicated in modern climate change¹. The long-term variations of IPWP OHC and their effect on monsoonal hydroclimate are, however, not fully explored. Here, by combining geochemical proxies and transient climate simulations, we show that changes of IPWP subsurface OHC (0-200 m) over the past 360,000 years exhibit dominant precession and weaker obliquity cycles following the changes in meridional insolation gradients. Only 30-40% of the deglacial increases are, however, related to changes in ice volume. On the precessional band, higher subsurface OHC correlates with oxygen isotope enrichments in IPWP surface water and

concomitant depletion in East Asian precipitation as recorded in Chinese speleothems. Using isotope-enabled air-sea coupled model, we suggest that on precessional timescale, variations in IPWP subsurface OHC, more than surface temperatures, act to amplify the ocean-continent hydrological linkage via moisture / latent heat convergence. Thus, from energetic viewpoint, this coupling of OHC and monsoon variations, both coordinated by insolation changes at orbital timescales, is critical for regulating the global hydroclimate.

A key feature of anthropogenic climate change is that heat associated with the present energy imbalance is mainly (~90 %) absorbed by the world's oceans¹. Indeed, a substantial slowdown in surface warming between 2002 and 2012²⁻³ has been attributed to an increased subsurface ocean heat uptake, through increased subduction in the Pacific shallow overturning cells and enhanced heat convergence in the equatorial thermocline⁴. Increased upper ocean heat content (OHC) might have fueled and intensified La Niña, monsoon and tropical cyclone activities during the latest decade⁵⁻⁷. Given the time-limited and transient response seen in modern observations (i.e., the shift in the 1970s), we show here that further knowledge of the relationships between variations in equatorial Pacific OHC and tropical hydroclimate can be gained from paleoclimate records⁸⁻⁹.

The Indo-Pacific Warm Pool (IPWP), defined by sea surface temperature (SST) of >28 °C (Fig. 1a), is the largest reservoir of warm water on Earth and serves as a "steam and heat engine" for global climate today, and its upper OHC plays a particularly significant role in the energy flow and hydrological cycles of the Earth's surface system¹⁰. Observations, reanalysis, and model simulations suggest that changes in the western Pacific OHC above 200 m water depth dominate both the tropical and global OHC during El Niño Southern Oscillation (ENSO) (Fig. 1b) and redistribute heat in the ocean and moisture in the atmosphere¹¹⁻¹². On interannual to

multi-decadal timescales, the IPWP upper OHC above 26°C (D26)⁷ or 20°C (D20)⁵ isotherms, rather than the SST, has been viewed as a more effective predictor of Asian monsoon precipitation⁶ and its isotope behaviors through atmospheric teleconnections associated with ENSO¹³⁻¹⁴. For example, interannual La Niña events are accompanied with increased upper OHC above 200 m or above D20 isotherm, and negative shifts of the precipitation $\delta^{18}O$ ($\delta^{18}O_p$) in East Asia (Fig. 1; Extended Data Fig. 1), indicating that ENSO-related IPWP OHC anomalies can greatly intensify Asian summer monsoon precipitation through associated ocean-continent moisture/moist-static-energy transport^{10, 12}.

52

53

54

55

56

57

58

59

60

61

62

63

64

65

66

67

68

69

70

71

72

73

74

75

76

Records of OHC in the equatorial Pacific beyond the instrumental observations show a substantial decrease from the early (11,000-8,000 years ago) to late Holocene (past 4,000 years)¹⁵⁻¹⁶, even though during the same time global surface temperatures did not change much. A recent study reports that more heat was stored in intermediate and thermocline waters of the South China Sea during the last deglaciation (20,000-11,000 years ago) and was released upward to the sea surface during the Holocene¹⁷. This suggests that the upper OHC anomaly is a recurring phenomenon in the low-latitude Indo-Pacific and may greatly regulate Asian monsoonal energy and moisture changes on orbital timescales 12, 18. However, previous studies are confined to the last 20,000 years, limiting our understanding of the upper OHC modulation of monsoon responses to orbital-driven changes in solar insolation or CO₂, in which the radiative heating driven OHC and associated hydrological changes may provide long-term boundary constrains for future climate projection. Here we reconstructed upper (0-200 m) OHC in the IPWP for the last 360,000 years, based on the SST and thermocline water temperatures (TWT) estimated by Mg/Ca ratios of foraminiferal shells from 10 deep-sea sediment cores. We combine the resulting OHC reconstruction and associated seawater and atmospheric moisture δ¹⁸O with climate model simulations to investigate orbital-scale OHC-monsoon relationships, underlying mechanisms, and implications for global hydroclimate changes.

77

78

79

80

81

82

83

84

85

86

87

88

89

90

91

92

93

94

95

96

97

98

99

100

101

Different SST and TWT variation patterns

Variation in the upper OHC over the equatorial Pacific is largely determined by the known ENSO-related tilting of the thermocline¹⁹. Because past changes in TWT are much larger than SST changes^{15, 20}, understanding the role of the thermocline is critical for inferring past changes in the upper OHC. Based on plankton tow²¹ and core-top sediment²² samples from the IPWP, the calcification depth of the species Globigerinoides ruber sensu stricto and Pulleniatina obliquiloculata are estimated at 25-95 m (mixed layer) and 110-160 m water depth (upper thermocline), respectively. Therefore, we reconstructed SST and TWT based on the Mg/Ca ratios in planktic foraminiferal shells of G. ruber and P. obliquiloculata, respectively, from 5 sediment cores MD10-3340, KX21-2, SO18480-3 (records of the last 25,000 years in the three cores have been published²³), ODP807, and MD98-2162 (SST only) (age models refer to Methods and Extended Data Fig. 2). The average time resolution ranges from 140 yrs/sample to 930 yrs/sample, except for core ODP807 (2910 yrs/sample). The data of 5 newly studied cores and 5 previously published records in the IPWP, spanning the last 400,000 years, are used in this study to establish the SST and TWT stacks (Fig. 2). The SSTs of five newly studied cores display a typical 100-kyr glacial-interglacial cycle, whereas the TWT of four newly studied cores show a clear precession cycle over the last 400,000 years (Extended Data Fig. 3). It is worth noting that the TWTs at three equatorial Pacific sites (KX21-2, GeoB17426 and MD10-3340) show a stronger signal in the obliquity than in the precession band, while precession dominates the other six sites (Fig. 1a; Extended Data Fig. 4). We constructed stacks of SST (10 sites) and TWT (9 sites), after interpolating the original records to an even time-step of 500 years. The SST stack ranges from 26.2 to 30.1 °C with an average of 27.6 °C, displaying a dominant 100-kyr cycle superimposed by high signalto-noise precession and obliquity fluctuations (Fig. 2a, f); the TWT stack ranges from 19.8 to 25.0 °C with an average of 21.7 °C, dominated by precession and (relative weak) obliquity cycles (Fig. 2b, g). Therefore, the upper ocean temperature changes in the IPWP show two different and independent first-order patterns: (1) the SST pattern with a dominant ~100-kyr cycle (Fig. 2a), and (2) the TWT pattern with a dominant 23-kyr cycle (Fig. 2b). The SST is likely responding to greenhouse gas²⁴ and/or polar ice forcing, with a clear glacial-interglacial rhythm, whereas the more variable TWT is likely responding to low-latitude climate and upper ocean dynamics, mainly forced by precession-driven insolation changes or precession-obliquity hybrid meridional insolation gradients in the tropics^{20, 25}.

Hybrid precession and obliquity driving

We used the Mg/Ca-derived temperatures of *G. ruber* and *P. obliquiloculata* to represent mixed layer and upper thermocline temperatures constrained by the shallowest D26 (70 m) and the deepest D20 isotherms (188 m), respectively (Extended Data Fig. 5), for calculating the upper OHC (in Joules m⁻²) above 200 m. The error range of this OHC estimation averages 0.08×10^{10} J/m² (1σ) or 0.11×10^{10} J/m² (2σ) as determined by error propagation (Methods). The proxy reconstructed upper OHC stack of the IPWP, based on the SST and TWT stacks, varies from 1.83×10^{10} J m⁻² to 2.28×10^{10} J m⁻² over the last 360,000 years (Fig. 2c). The proxy reconstruction is generally comparable with the simulated annual mean upper OHC changes from the Community Earth System Model 1.0.4 (CESM), in terms of both the amplitude and the pattern of variations on the precessional band, over the past 300,000 years. Filter and spectrum analyses confirm the dominance of 23-kyr precessional cycle in the reconstructed and simulated upper OHC, which dominates monsoonal precipitation records (Fig. 2c, h). The upper OHC increases while the IPWP thermocline deepens at precession minima and vice versa, indicating that the upper OHC of the IPWP, mainly regulated by the TWT, is driven by the precession-forced changes in low-latitude insolation.

In addition to the dominant precession cycle, the upper OHC of the IPWP also shows a significant obliquity cycle (Fig. 2h), which manifests as extreme spikes, culminating at the earliest interglacials (early MIS 1, MIS 5.5 and MIS 9.3 with magnitudes of 0.29×10^{10} J/m², 0.35×10^{10} J/m² and 0.42×10^{10} J/m², respectively) when obliquity maxima (O_{max}) and precession minima (P_{min}) simultaneously occur (Fig. 2c, d). These OHC spikes are synchronous with peaks in the Summer Interhemispheric Tropical Insolation Gradient (SITIG²⁵, June insolation difference between 23°N and 23S°). As showcased by the linear combination of the normalized obliquity and precession (Fig. 2e), these SITIG peaks may reflect the interactions between high and low latitudes and their potential effects on the drastic OHC changes over the glacial terminations to earliest interglacial stages.

As an intermedium of high and low latitudes, obliquity has been identified as an important driver of ice sheet and CO₂²⁵. Our results indicate that the alignment of obliquity and precession (i.e., the O_{max} and P_{min} aligned insolation maxima) bridges those OHC spikes between the IPWP upper OHC and the southern hemispheric temperature records²⁶. In modern climate, the western equatorial Pacific thermocline water originates from the basin-wide shallow overturning circulation of the Pacific Ocean, which is fed by the subduction of relatively saline, warm surface waters in the subtropical North and South Pacific²⁷. This physical process was effective in the late Quaternary and was more vigorously accomplished by the subtropical-to-tropical thermocline circulation in the South Pacific²⁰. The upper OHC stack of the IPWP, surface air temperature (SAT) from EDC ice core record²⁸ and Mg/Ca-SST record from the extratropical Southwest Pacific (MD2120 SST)²⁶ show very similar changes over the last 360,000 years, and they are all significantly coherent in the obliquity band (Extended Data Fig. 6). The cross spectral (relative to the obliquity parameter) analyses reveal that the changes in the IPWP OHC stack, TWT stack of the Ontong-Java Plateau (OJP) sites, EDC SAT and MD2120 SST are almost in phase (within age uncertainties) in the obliquity band (Extended Data Fig. 6e). The

relatively warmer mid-latitude southern Pacific SST and thereby enhanced warm water transport of shallow overturning circulation at obliquity maxima may have further strengthened the IPWP TWT/OHC spikes at precession minima²⁹.

152

153

154

155

156

157

158

159

160

161

162

163

164

165

166

167

168

169

170

171

172

173

174

175

176

The dominant precession feature and spikes (at MIS 1 and 5.5) of proxy-reconstructed upper OHC are also reproduced by our orbital- and greenhouse gases (GHG)-forced simulations of the Community Earth System Model 1.0.4 (CESM) over the past 300,000 years (Fig. 2c; Methods), although with smaller magnitudes (0.14×10¹⁰ J/m² and 0.22×10¹⁰ J/m² for MIS 1 and 5.5, respectively). This implies that at least half of the magnitude of these OHC spikes are explained by orbital insolation (SITIG) and atmospheric CO₂, while the remnant could be attributed to insolation-driven ice volume changes (not included in the CESM model). The latent heat absorbed by ice sheet melting water, for instance, would be input into the ocean and increase global mean ocean temperature (MOT) during the last deglaciation⁸⁻⁹. The noble-gas reconstructed MOT increases by 2.01 °C and 1.38 °C at MIS 1 and MIS 5.5 (Extended Data Fig. 6b), which may increase the IPWP upper OHC by 0.17×10^{10} and 0.12×10^{10} J/m², respectively, and largely complement the missing change in our CESM simulations relative to the proxy reconstructions. Interestingly, the early MIS 7.5, a 'failed' interglacial in terms of much weaker increases of MOT (0.28 °C) and IPWP OHC (0.2×10¹⁰ J/m²), is well simulated by the CESM (0.18×10¹⁰ J/m²) because of slighter ice volume changes³⁰. Therefore, only about 30 % to 40 % of upper OHC increases from the last three deglaciations towards earliest interglacials are related to changes in ice volume.

Therefore, the concurrent IPWP TWT/OHC spikes culminating at the earliest interglacial stages, most significantly observed in the OJP sites, are likely related to the precession and obliquity insolation-driven meridional heat transport anomalies in the upper ocean. This hybrid forcing concept^{25, 30} could explain the orbital-forcing controlled upper OHC of the IPWP, indicating that the precession changes of upper OHC is modulated by the obliquity-driven

meridional insolation gradients and are also sensitive to the climate changes at higher latitudes that are forced mainly by obliquity²⁶. Our upper OHC records indicate that precession, obliquity, or their combination could have paced the late Pleistocene deglaciations³⁰, for more than 60 % of their amplitude of changes, through the oceanic heat uptake and release in the IPWP.

181

182

183

184

185

186

187

188

189

190

191

192

193

194

195

196

197

198

199

200

201

177

178

179

180

OHC-regulated monsoon moisture transport

The IPWP acts as a heat engine and builds up large OHC anomalies that energetically determine the Asian monsoonal hydrological budgets through ENSO and Indian Ocean dipole (IOD) in the modern world^{6, 11-14}. To investigate orbital scale hydrological changes related to the upper OHC of the IPWP, the residual δ^{18} O of surface seawater (δ^{18} O_{sw}, with the ice-volume effect removed) was calculated from the δ^{18} O of mixed layer-dwelling species G. ruber (Methods). Additionally, we simulated the annual mean surface seawater $\delta^{18}O_{sw}$ of the IPWP by a water isotope (δ^{18} O)-enabled air-sea coupled climate model GISS ModelE2-R (Methods). Both the stacked $\delta^{18}O_{sw}$ of 10 sediment cores and simulated $\delta^{18}O_{sw}$ of the IPWP show a dominant 23kyr cycle with heavier $\delta^{18}O_{sw}$ values at P_{min} (Fig. 3b). In our GISS ModelE2-R transient experiment, the precipitation $\delta^{18}O$ ($\delta^{18}O_p$) of East Asia is consistent with the composite record of Chinese speleothem $\delta^{18}O^{31}$, a widely used proxy for changes in the strength of the East Asian summer monsoon (EASM) circulation (Fig. 3c). But both the speleothem δ^{18} O stack and simulated δ^{18} O_p, showing a dominant precession cycle of 23-kyr, are anti-correlated with the precessional change of $\delta^{18}O_{sw}$ stack in the IPWP. When the IPWP $\delta^{18}O_{sw}$ increased at P_{min} , Chinese speleothem $\delta^{18}O$ decreased (Fig. 3b, c)³². This enlarged δ^{18} O gradient between ocean and continent ($\Delta\delta^{18}$ O_{ocean-continent}; Extended Data Figs. 7-8) compares well with another indicator of the intensity of low-latitude hydrological cycle (Dole

The upper OHC and $\delta^{18}O_{sw}$ share a common dominant precession cycle with Chinese

Effect)³³, but more purely represents the ocean-continent oxygen isotope fractionation.

speleothem δ^{18} O, but with stronger obliquity imprints that might arise from the obliquity-driven subtropical changes (Fig. 3d). In the precession band, Chinese speleothem δ^{18} O (reversed) is significantly coherent and almost in phase with the OHC and δ^{18} O_{sw} (Fig. 3e, f), lagging the precession parameter minimum (boreal summer insolation maximum) by 43° (~2750 years). A higher OHC of the IPWP is correlated with a stronger East Asian summer monsoon at precession minima, thermodynamically via a greater transport of moisture from ocean to continent that produces depleted δ^{18} O values in Chinese speleothems³⁴ (Fig. 3a, c).

202

203

204

205

206

207

208

209

210

211

212

213

214

215

216

217

218

219

220

221

222

223

224

225

226

Previous studies proposed that Chinese speleothem $\delta^{18}O$ does not reflect changes in the monsoon strength, but in the alternation of monsoonal moisture source, with the Indian Ocean being the most distant and ¹⁸O-depleted source and the subtropical north Pacific the most proximal and ¹⁸O-enriched source³⁵. In contrast, recent modelling studies argued that the depletion of Asian continent $\delta^{18}O_p$ at P_{min} reflects stronger summer monsoon circulation, which enhances transport and rainout of moisture evaporated from the tropical Indian and Pacific oceans³⁶. Our transient simulations further suggest that Pacific-originated moisture and associated thermodynamics could contribute a larger proportion of the negative shift of Chinese speleothem δ^{18} O at precessional band (Fig. 4a). The dominant role of Pacific-sourced moisture on East Asian precipitation has been recently substantiated by modern observations³⁷ and acts probably through ENSO-like atmospheric teleconnections³⁸ or tropical cyclone activities around the subtropical high-pressure^{39, 40}. In our transient experiments, both annual mean $\delta^{18}O_{sw}$ and δ¹⁸O_p increase at P_{min} in the remote Pacific moisture source regions (Fig. 4b-c; Extended Data Fig. 8), mainly due to local boreal summer precipitation of relatively positive $\delta^{18}O_p$ and more evaporation of negative water vapor $\delta^{18}O$ ($\delta^{18}O_{\text{evap}}$) (Fig. 4e; Extended Data Fig. 9). More δ^{18} O-depleted precipitation occurs in the Asian continent due to increased rainout along the tracks of the Asian summer monsoon, consistent with intensified Asian summer monsoon and Walker circulations at P_{min} (Fig. 4; Extended Data Fig. 8).

The precessional forced IPWP upper OHC can be explained from a viewpoint of atmospheric-oceanic coupled energy transport⁴¹. During the precessional minima, increased meridional SITIG sets the strength of atmospheric Hadley circulation. A stronger and northward shift of zonal mean position of Intertropical Convergence Zone (ITCZ) is compensated by enhanced subtropical high-pressure anomalies in the Indian-Pacific Oceans (Extended Data Fig. 9)⁴². These subtropical atmospheric anomalies will warm the IPWP thermocline through meridional ocean heat transport of Subtropical-to-Tropical Circulation^{20, 43}. Then the relationship between IPWP upper OHC and ocean-continent moisture transport can be explained in the context of atmospheric moist static energy theory⁴⁴.

In modern climate, IPWP upper OHC is largely determined by changes in the tilt of the tropical thermocline, and therefore is taken as a more sensitive indicator of ENSO⁵ and EASM than SST^{6, 39, 40}, exerting strong feedback on Hadley / monsoon and Walker circulations by modulating the surface SST gradient and moist static energy⁴⁵. In our precessional forced transient simulations, accompanying with an increase of IPWP OHC by 0.1×10¹⁰ J/m², increases would be seen in the latent heat release (by 0.036×10¹⁰ J/m²) and the precipitation rate (by 0.4 mm/day) of EASM (Extended Data Fig. 8c). Additional CESM equilibrium simulations under different air-sea coupled configurations also highlight the amplification effect of ocean heat transport on the moisture transport of EASM under precessional forcing (Extended Data Fig. 10). Along the equatorial Pacific, increased IPWP OHC and associated air-sea interactions further result in stronger Walker Circulation and zonal La Nina-like SST gradient anomalies⁴⁶. In such an IPWP-monsoon linkage, the warmed IPWP with relatively lower surface pressure serves as an atmospheric 'water tower' by converging more oceanic moisture (and latent heat) from the remote Pacific source (i.e. the central equatorial Pacific, subtropical south and north Pacific), and transferring to the adjacent Asian continent monsoon regions. It is this remote moisture convergence effect and upstream convective precipitation rainout effect that amplify the Pacific-to-Asian continent oxygen isotope fractionation.

The role of IPWP upper OHC as an amplifier and a better predictor of EASM than SST is evident from the fact that the OHC exhibits stronger precessional variance, which is the dominant period in the Chinese speleothem records of EASM³¹ but lacked in the SST records. Our results are also broadly consistent with the modern observations and Holocene trends in land moisture and ocean salinity, with warming over the ocean and an increase in continental precipitation at the expense of maritime precipitation⁴⁷. That is, the upper OHC of the IPWP and associated air-sea interactions critically regulates the ocean-continent hydroclimate dynamics and thus moisture transport and water isotope fractionation between the Pacific Ocean and East Asia from interannual¹³ to orbital timescales. While the seasonal changes of solar insolation and ocean-continent thermal contrasts are two basic drivers of global monsoon system, our results further emphasize the amplification role of dynamical oceanic feedbacks on the Asian summer monsoon under orbital insolation forcing. The coupled heat storage of the equatorial Pacific thermocline and low-latitude hydrological changes may greatly help us to project the ocean-atmosphere-continent hydroclimate changes under future warming.

Online content

Any methods, additional references, extended data, source data, supplementary information, acknowledgements; details of author contributions and competing interests; and statements of data and code availability are available at https://doi.org/10.1038.....

- Cheng, L. et al. Improved estimates of ocean heat content from 1960 to 2015. *Sci. Adv.* 3(3), e1601545
 (2017).
- 275 2. Kosaka, Y. & Xie S. P. Recent global-warming hiatus tied to equatorial Pacific surface cooling. *Nature* 501, 403-407 (2013).
- 277 3. Chen, X. & Tung, K. K. Varying planetary heat sink led to global-warming slowdown and acceleration.

- 278 Science **345**, 897-903 (2014).
- 4. England, H. M. et al. Recent intensification of wind-driven circulation in the Pacific and the ongoing
- 280 warming hiatus. *Nat. Clim. Change* **4**, 222-227 (2014).
- 5. Izumo, T., Lengaigne, M., Vialard, J., Suresh, I. & Planton, Y. On the physical interpretation of the lead
- relation between Warm Water Volume and the El Niño Southern Oscillation. Clim. Dyn. 52(5), 2923-
- 283 2942 (2019).
- 284 6. Rajeevan, M. & McPhaden, M. J. Tropical Pacific upper ocean heat content variations and Indian
- summer monsoon rainfall. *Geophys. Res. Lett.* **31**, L18203, doi:10.1029/2004GL020631 (2004).
- 286 7. Lin, I. I., Goni, G., Knaff, J. A., Forbes, C. & Ali, M. M. Ocean heat content for tropical cyclone intensity
- forecasting and its impact on storm surge. *Natural Hazards* **66(3)**, 1481-1500 (2013).
- 8. Bereiter, B., Shackleton, S., Baggenstos, D., Kawamura, K. & Severinghaus, J. Mean global ocean
- temperatures during the last glacial transition. *Nature* **553**, 39-44 (2018).
- 290 9. Haeberli, M. et al. Snapshots of mean ocean temperature over the last 700 000 years using noble gases
- 291 in the EPICA Dome C ice core. *Clim. Past* **17(2)**, 843-867 (2021).
- 292 10. Mayer, M., Haimberger, L. & Balmaseda, M. A. On the energy exchange between tropical ocean basins
- related to ENSO. J. Clim. 27(17), 6393-6403 (2014).
- 294 11. Schneider, T., Bischoff, T. & Haug, G. H. Migrations and dynamics of the intertropical convergence
- 295 zone. *Nature* **513**, 45-53 (2014).
- 296 12. Biasutti, M. et al. Global energetics and local physics as drivers of past, present and future monsoons.
- 297 *Nature Geosci.* **11**, 392-400 (2018).
- 298 13. Yang, H., Johnson, K. R., Griffiths, M. L. & Yoshimura, K. Interannual controls on oxygen isotope
- variability in Asian monsoon precipitation and implications for paleoclimate reconstructions. *J. Geophys.*
- 300 Res. Atmos. **121**(14), 8410-8428 (2016).
- 301 14. Cai, Z., Tian, L. & Bowen, G. J. Influence of recent climate shifts on the relationship between ENSO
- and Asian Monsoon precipitation oxygen isotope ratios. *J. Geophys. Res. Atmos.* **124**, 7825-7835 (2019).
- 303 15. Rosenthal, Y., Linsley, B. K. & Oppo, D. W. Pacific Ocean heat content during the past 10,000 years.
- 304 *Science* **342**, 617-621 (2013).
- 305 16. Kalansky, J., Rosenthal, Y., Herbert, T., Bova, S., & Altabet, M. Southern Ocean contributions to the
- eastern Equatorial Pacific heat content during the Holocene. Earth Planet. Sci. Lett. 424, 158-167 (2015).

- 307 17. Yang, Y., Xiang, R., Zhang, L., Zhong, F., & Zhang, M. Is the upward release of intermediate ocean heat
- content a possible engine for low-latitude processes? *Geology* **48(6)**, 579-583 (2020).
- 309 18. Jalihal, C., Bosmans, J. H. C., Srinivasan, J., & Chakraborty, A. The response of tropical precipitation
- 310 to Earth's precession: the role of energy fluxes and vertical stability. *Clim. Past* **15**(2), 449–462 (2019).
- 311 19. Roemmich, D. & Gilson, J. The global ocean imprint of ENSO. *Geophys. Res. Lett.* **38**, L13606 (2011).
- 312 20. Jian, Z. et al., Half-precessional cycle of thermocline temperature in the western equatorial Pacific and
- 313 its bihemispheric dynamics. *Proc. Natl. Acad. Sci.* **117(13)**, 7044-7051 (2020).
- 314 21. Rippert, N. et al. Constraining foraminiferal calcification depths in the western Pacific warm pool. *Mar.*
- 315 *Micropaleontol.* **128**, 14-27 (2016).
- 316 22. Hollstein, M. et al. Stable oxygen isotopes and Mg/Ca in planktic foraminifera from modern surface
- sediments of the western Pacific warm pool: Implications for thermocline reconstructions.
- 318 *Paleoceanography* **32**, 1174-1194 (2017).
- 319 23. Dang, H. et al. Pacific Warm Pool sub-surface heat sequestration modulated Walker Circulation and
- 320 ENSO activity during the Holocene. Sci. Adv. 6(42), eabc0402 (2020).
- 321 24. Lea, D. W. The 100,000-yr cycle in tropical SST, greenhouse forcing, and climate sensitivity. *J. Clim.*
- **17**, 2170-2179 (2004).
- 323 25. Kuechler, R. R., Dupont, L. M. & Schefuß, E. Hybrid insolation forcing of Pliocene monsoon dynamics
- 324 in West Africa. *Clim. Past* **14**, 73-84 (2018).
- 325 26. Pahnke, K., Zahn, R., Elderfield, H. & Schulz, M. 340,000-Year centennial-scale marine record of
- 326 Southern Hemisphere climatic oscillation. *Science* **301**, 948-952 (2003).
- 327 27. Graffino, G., Farneti, R., Kucharski, F., & Molteni, F. The effect of wind stress anomalies and location
- in driving Pacific Subtropical cells and tropical climate. J. Clim. 32(5), 1641-1660 (2019).
- 329 28. Jouzel, J. et al. Orbital and Millennial Antarctic Climate Variability over the Past 800,000 Years. Science
- **330 317**, 793-797 (2007).
- 331 29. Hollstein, M. et al. The impact of astronomical forcing on surface and thermocline variability within the
- Western Pacific Warm Pool over the past 160 kyr. *Paleoceanogr. Paleoclimat.* **35(6)**, e2019PA003832
- 333 (2020).
- 334 30. Huybers, P. Combined obliquity and precession pacing of late Pleistocene deglaciations. *Nature* **480**,
- 335 229-232 (2011).

- 336 31. Cheng, H. et al. The Asian monsoon over the past 640,000 years and ice age terminations. *Nature* 534,
- 337 640-646 (2016).
- 338 32. Battisti, D. S., Ding, Q. & Roe, G. H. Coherent pan-Asian climatic and isotopic response to orbital
- forcing of tropical insolation, J. Geophys. Res. Atmos. 119, 11997-12020 (2014).
- 340 33. Huang, E. et al. Dole effect as a measurement of the low-latitude hydrological cycle over the past 800
- 341 ka. *Sci. Adv.* **6(41)**, eaba4823 (2020).
- 342 34. Bosmans, J. H. C. et al. Response of the Asian summer monsoons to idealized precession and obliquity
- 343 forcing in a set of GCMs. *Quat. Sci. Rev.* **188**, 121-135 (2018).
- 344 35. Baker, A. J. et al. Seasonality of westerly moisture transport in the East Asian summer monsoon and its
- implications for interpreting precipitation δ^{18} O. J. Geophys. Res. Atmos. 120(12), 5850-5862 (2015).
- 36. Hu, J., Emile-Geay, J., Tabor, C., Nusbaumer, J. & Partin, J. Deciphering oxygen isotope records from
- Chinese speleothems with an isotope-enabled climate model. *Paleoceanogr. Paleoclimat.* **34**, 2098-2112
- 348 (2019).
- 349 37. Shi, Y., Jiang, Z., Liu, Z. & Li, L. A Lagrangian analysis of water vapor sources and pathways for
- precipitation in East China in different stages of the East Asian summer monsoon. J. Clim. 33(3), 977-
- 351 992 (2020).
- 352 38. Fasullo, J. & Webster, P. J. Hydrological Signatures Relating the Asian Summer Monsoon and ENSO.
- 353 *J. Clim.* **15(21)**, 3082-3095 (2002).
- 354 39. Ling, S. N. & Lu, R. Y. Tropical cyclones over the western North Pacific strengthen the East Asia-Pacific
- 355 pattern during summer. *Adv. Atmos. Sci.* **39**(2): 249-259 (2022).
- 356 40. Cheng, T. F., Lu, M. & Dai, L. Moisture channels and pre-existing weather systems for East Asian rain
- 357 belts. npj Clim. Atmos. Sci. 4(1), 1-13 (2021).
- 358 41. Schneider, T. Feedback of atmosphere-ocean coupling on shifts of the Intertropical Convergence Zone.
- 359 Geophys. Res. Lett. 44, 11644-11653 (2017).
- 360 42. Merlis, T. M., Schneider, T., Bordoni, S. & Eisenman, I. The tropical precipitation response to orbital
- 361 precession. J. Clim. **26(6)**, 2010-2021 (2013).
- 362 43. Vallis, G. K. & Farneti, R. Meridional energy transport in the coupled atmosphere-ocean system: Scaling
- and numerical experiments. *Quart. J. Roy. Meteor. Soc.* **135(644)**, 1643-1660 (2009).

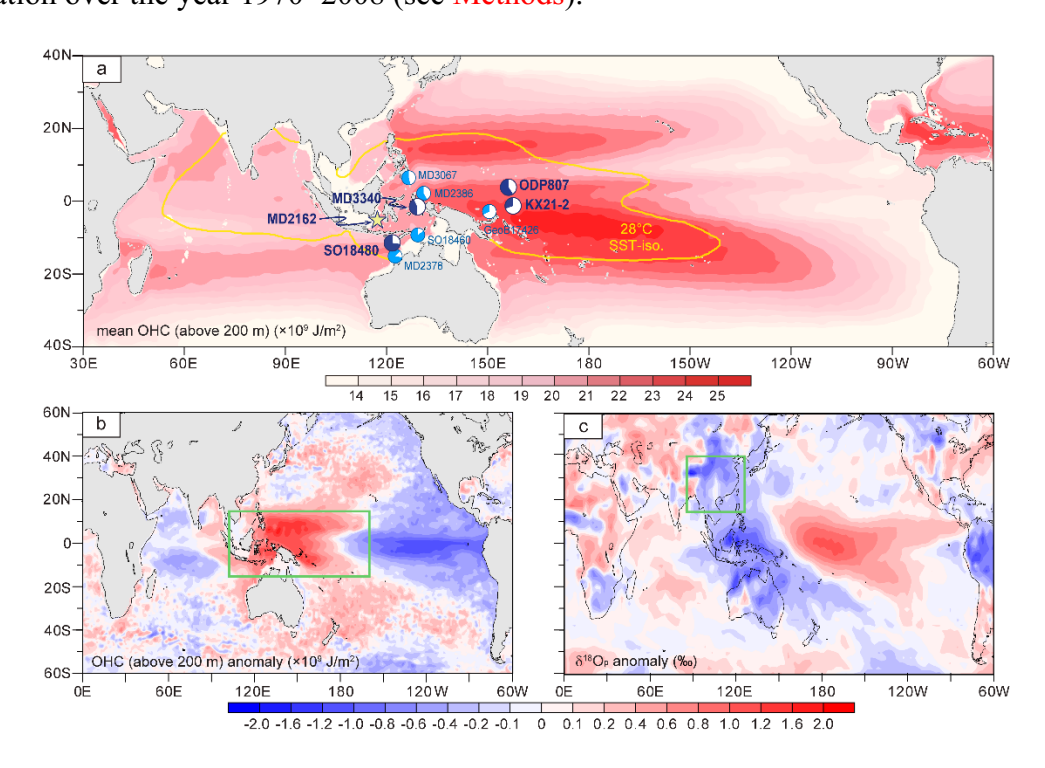
- 364 44. Hill, S. A. Theories for past and future monsoon rainfall changes. Curr. Clim. Change Rep. 5(3), 160-
- 365 171 (2019).

- 366 45. Lutsko, N. J., Marshall, J., & Green, B. Modulation of monsoon circulations by cross-equatorial ocean
- 367 heat transport. *J. Clim.* **32**(12), 3471-3485 (2019).
- 368 46. Wang, Y. et al. Precessional Forced Zonal Triple-Pole Anomalies in the Tropical Pacific Annual Cycle.
- 369 *J. Clim.* **32(21)**, 7369-7402 (2019).
- 370 47. Oppo, D. W., Schmidt, G.A. & LeGrande, A. N. Seawater isotope constrains on tropical hydrology
- 371 during the Holocene. *Geophys. Res. Lett.* **34**, L13701 (2007).

FIGURE CAPTIONS

Fig. 1 | Modern IPWP upper OHC and its influence on precipitation δ^{18} O.

(a) The IPWP defined by the SST isotherm of 28 °C (yellow contour) is shown with annual mean climatological OHC (colored) above 200 m water depth, and site locations of the 10 sediment cores are marked as colored pies (light blue: previous studies; dark blue: this study; star: core MD98-2162 with only an SST record), in which the blue and white sectors of each pie demonstrate the % ratios of precession and obliquity of TWT spectrum (detailed in Extended Data Fig. 4). (b) modern La Niña-associated annual mean OHC anomalies above 200 m water depth from SODA reanalysis dataset, shown as regression coefficients against normalized time series of Southern Oscillation Index (SOI). (c) is the same as (b) but for La Niña-associated annual mean precipitation δ^{18} O (δ^{18} O_p) changes from the GISS historical simulation over the year 1970~2008 (see Methods).



388 Fig. 2 | Precession and obliquity changes in the proxy reconstructed and modelled IPWP 389 upper OHC. 390 (a)-(b) paleo-proxy based IPWP SST and TWT stacks are compared with the global stacked benthic foraminifera δ^{18} O record (LR04 δ^{18} O_{benthic}) and precession parameter, respectively. (c) 391 392 IPWP OHC stack reconstructed by proxy records (red) and the CESM-simulated IPWP OHC 393 (black), both shown as the anomaly relative to 0~3 ka average (Methods). (d) the precessional 394 (black) and obliquity (blue) parameters. (e) the Summer Interhemispheric Tropical Insolation 395 Gradient (SITIG, June insolation differences between 23°N and 23°S; pink) and the linear 396 combination of the normalized obliquity and precession (black dashed line). In (c)-(e), the 397 precession minima (P_{min}) and obliquity maxima (for peak interglacials) are shown in gray and 398 light purple vertical bars, respectively. Key marine isotope stages are shown above the records. 399 (f)-(h) spectral powers of IPWP stacked SST, TWT and OHC, calculated by the Redfit software 400 (window = rectangle, segments = 4, oversample = 3). Solid lines are the original spectral 401 amplitude (colored) and ratio relative to theoretical red noise (black), while dashed lines are 402 their 99 % confidence levels.

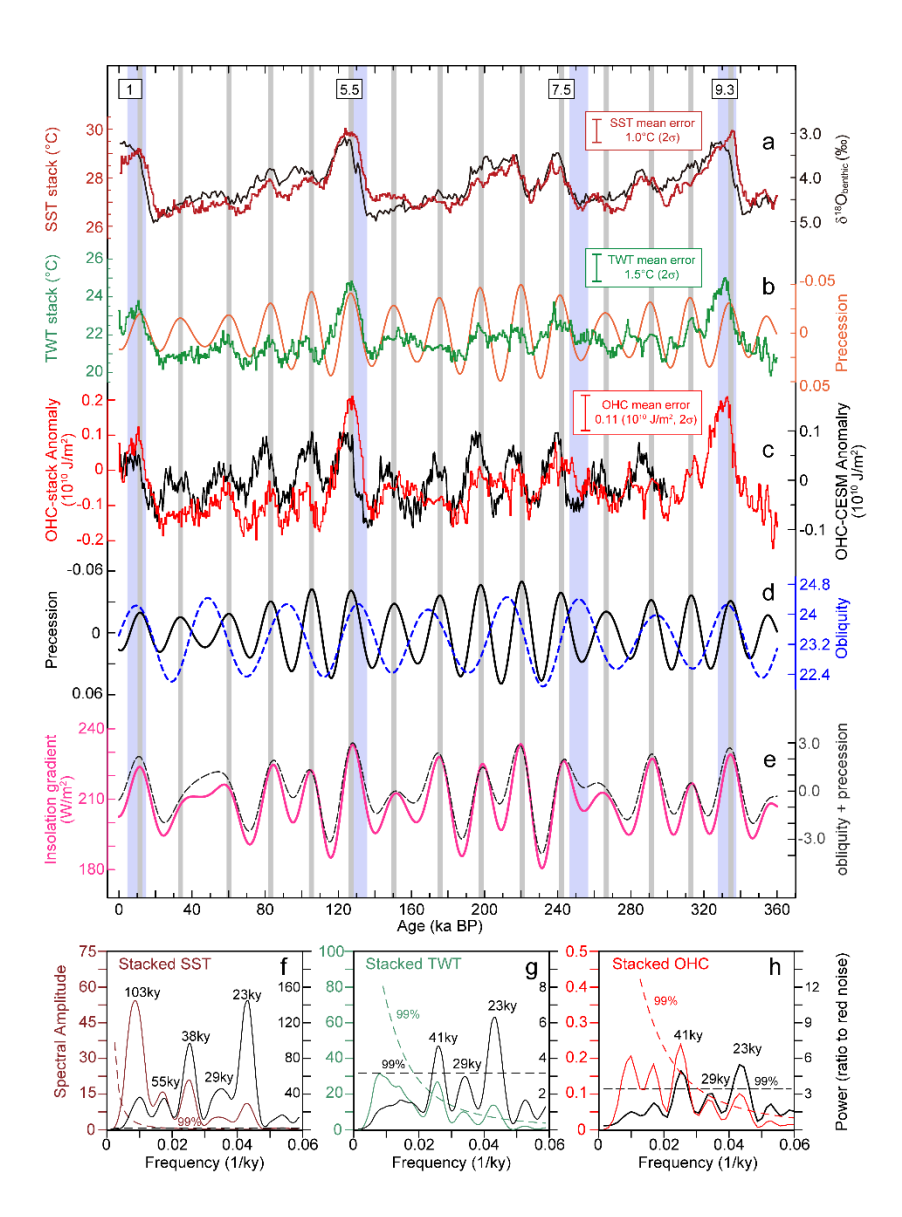


Fig. 3 | Precession dominated changes in the indices of low-latitude hydrological cycle.

Anomalies of proxy-based stacks of (a) IPWP OHC (red) and (b) IPWP surface water $\delta^{18}O$ ($\delta^{18}O_{sw}$, green), and (c) the Chinese speleothem $\delta^{18}O$ ($\delta^{18}O_{cave}$, blue), comparing with the GISS simulated anomalies (black lines) of annual mean $\delta^{18}O_{sw}$ over IPWP (b) and boreal summer (July-August-September, JAS) atmospheric precipitation $\delta^{18}O$ ($\delta^{18}O_p$) over East Asia (c) (spatial ranges shown in Fig. 4c). In (a)-(c), brown vertical bars indicate the minima of precession parameter (gray curves). (d) Spectrums for the IPWP OHC, $\delta^{18}O_{sw}$, and $\delta^{18}O_{cave}$. Cross spectrums of these three records relative to the precessional parameter maximum (P_{max}) are calculated as phase angles (e) and coherences (f). Note the phase-angle of speleothem $\delta^{18}O$ is reversed by 180° for better comparison.

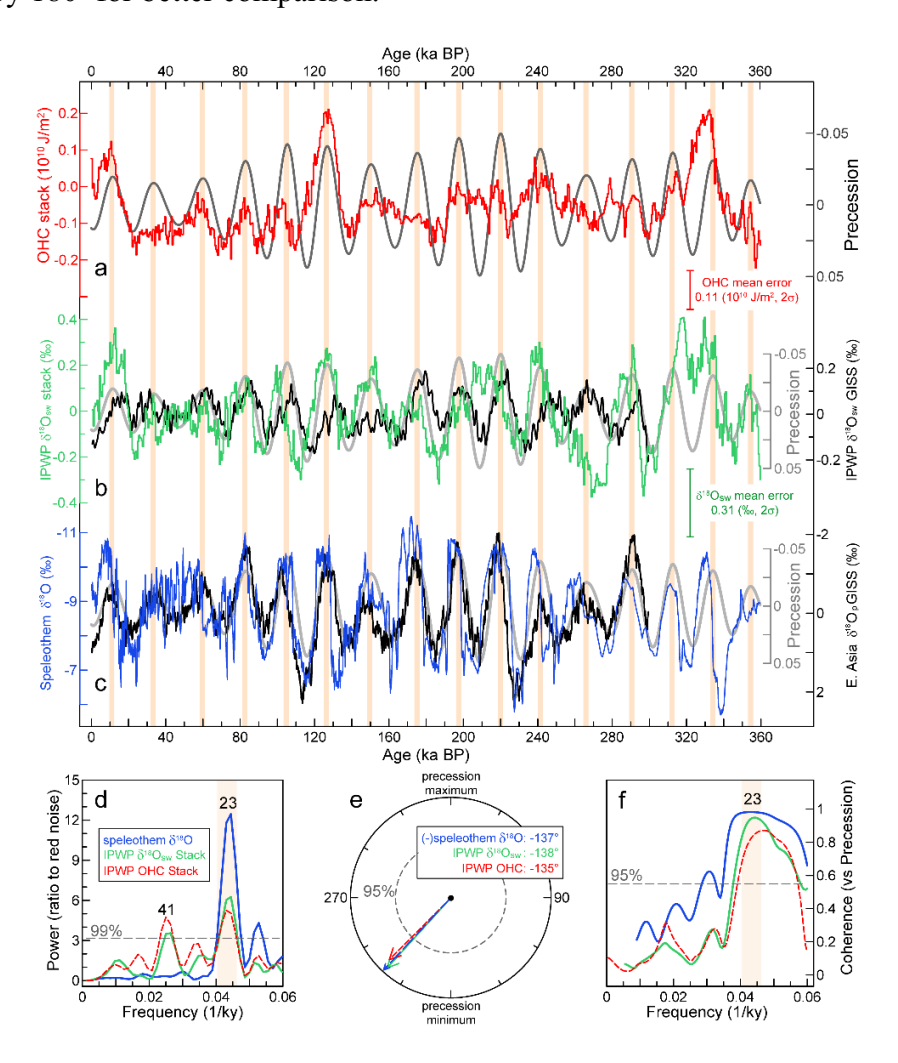


Fig. 4 | Ocean-continent δ^{18} O fractionation coupled with OHC and monsoon.

417

418

419

420

421

422

423

424

425

426

427

428

429

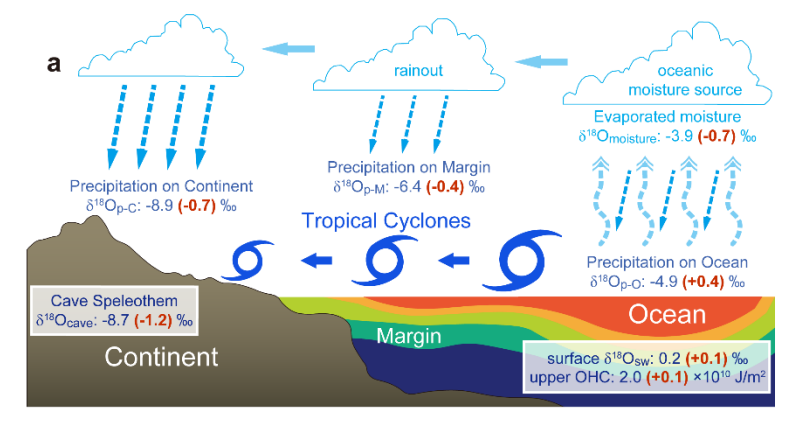
430

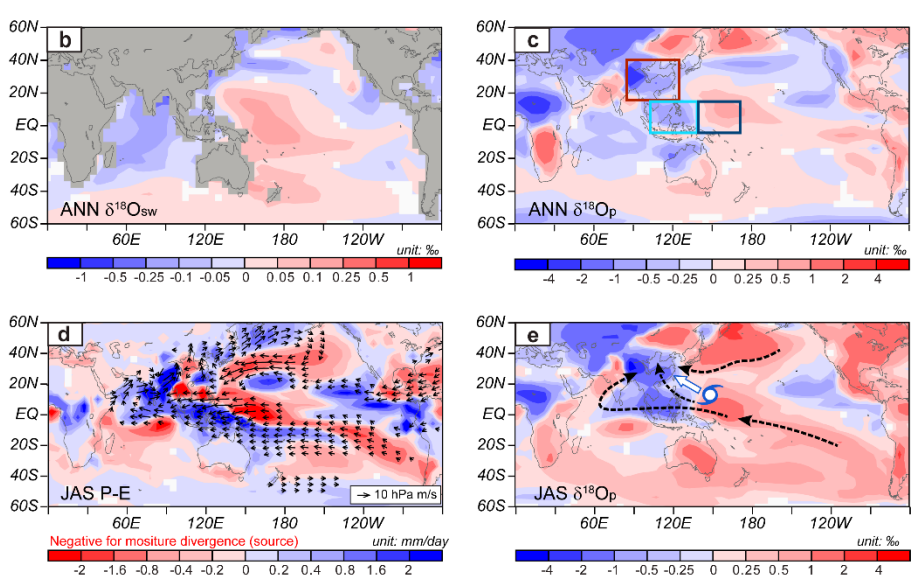
431

432

433

(a) Conceptual illustration of the moisture transport and $\delta^{18}O$ fractionation between the IPWP and Asian continent. Numbers are the climatological mean value (blue) and 1σ standard deviation (red; signs stand for anomalies at P_{min}), calculated for time series of OHC and $\delta^{18}O_{cave}$ (proxies in Fig. 3), and regionally averaged δ^{18} O of water vapor and precipitation (from GISS ghg experiment, areas for tropical Pacific Ocean, monsoonal margin and East Asia are shown in (c) by dark blue, shallow blue and brown boxes, respectively) (see Methods). (b)-(c) GISS simulated annual mean (ANN) $\delta^{18}O_{sw}$ and $\delta^{18}O_{p}$ anomalies at P_{min} (relative to P_{max}). Boxes in (c) mark the spatial ranges of IPWP (5°S-15°N, 140°E-170°E, dark blue), East Asia (15°N-40°N, 85°E-125°E, red) and the marginal region in-between (light blue). (d) Anomalies of boreal summer (JAS) precipitation-minus-evaporation (P-E, color shaded, negative values stand for local atmospheric moisture divergence or output) and vertical integrated atmospheric moisture transport flux (vectors) at P_{min} (relative to P_{max}). (e) JAS $\delta^{18}O_p$ anomalies at P_{min} (relative to P_{max}), overlapped with schematic pathways of moisture transport (black arrows for the mean circulation sketched from vectors in (d) and blue symbol and arrow for the contribution of tropical cyclones). White shading in (b)-(e) denotes areas not significant at 95 % confidence level of two-tail *t*-test.





Methods

436

437

438

439

440

441

442

443

444

445

446

447

448

449

450

451

452

453

454

455

456

457

458

459

460

Laboratory Measurements

For the Mg/Ca analyses, foraminiferal specimens from 2452 samples from five sediment core SO18480-3 (12°3.5'S, 121°39.0'E, water depth 2299 m), MD10-3340 (0°31.0'S, 128°43.5'E, water depth 1094 m), KX21-2 (1°25.0'S, 157°58.9'E, water depth 1897 m), ODP807 (3°36.4'N, 156°37.5'E, water depth 2804 m) and MD98-2162 (4°41.3'S, 117°54.2'E, water depth 1855 m) (Supplementary Information Table 1) are pretreated following the procedure described by Lea et al⁴⁸, but with additional checking and removing of potential contamination performed under a microscope. The Mg/Ca measurements (Supplementary Information Table 2) of 1947 samples from cores SO18480-3, MD10-3340, KX21-2 and ODP807 are conducted using an ICP-MS (Thermo VG-X7) at the State Key Laboratory of Marine Geology, Tongji University, with a mean reproducibility of 2.2 % for G. ruber (N=240) and 4.8 % for P. obliquiloculata (N=216), estimated by replicate measurements on aliquot samples (N: total replicates). The 505 samples of core MD98-2162 are analyzed (only for G. ruber) at the Department of Earth Science, University of California, Santa Barbara, using a Finnigan MAT Element-2 ICP-MS. The stable isotopic analysis of G. ruber (707 samples of Core SO18480-3) are carried out by a Finnigan MAT253 mass spectrometer equipped with an automatic carbonate preparation device (Kiel III) at the State Key Laboratory of Marine Geology, Tongji University. The isotopic results are calibrated to the Pee Dee Belemnite (PDB) scale via the China National standard NBS 19. The standard deviation is better than ± 0.07 % for δ^{18} O. The other 503 samples of core MD98-2162 are analyzed for δ^{18} O at the Department of Earth Science, University of California, Santa Barbara, by a Fisons Optima isotope ratio mass spectrometer with analytical precision of ± 0.06 %.

Proxy Reconstructions

The age models of the 10 cores are established by radiocarbon dates on mixed-layer dwelling planktic foraminiferal shells for the upper parts (\leq 40,000 years) and synchronized to the LR04 stack⁴⁹ based on their benthic foraminifera $\delta^{18}O^{20,\,29,\,50-54}$ or to *G. ruber* $\delta^{18}O$ of core MD01-2378⁵¹ based on their planktic foraminifera $\delta^{18}O^{55-56}$ (for cores SO18480-3 and MD98-2162) (Extended Data Fig. 2; Supplementary Information Table 2).

In this study, new data of 5 cores and published records^{20, 29, 50-51, 57-58} of another 5 cores are used for the SST and TWT stacks. Here, the SST is converted from the Mg/Ca of *G. ruber* shells by combining the Mg/Ca-SST equations (Mg/Ca = B×exp [A×SST]) developed by Dang et al⁵³ and by Hollstein et al²² with exponential coefficient A (0.097~0.099) and pre-exponents B (0.26~0.275) (Supplementary Information Table 1), adjusted for different sites to match their modern observed SST values. TWT is converted from the species-specific Mg/Ca-TWT equation of *P. obliquiloculata*⁵⁹. The errors of SST and TWT reconstruction, introduced by the Mg/Ca measurements and Mg/Ca-temperature calibrations⁶⁰, are estimated to be \pm 0.8 °C (1 σ , and 2 σ error \pm 1.0°C) and \pm 1.2°C (1 σ , and 2 σ error \pm 1.5°C), respectively.

The proxy reconstructed upper OHC above 200 m is calculated as follows:

477 OHC =
$$C_p * (\rho_1 * SST * dZ_1 + \rho_2 * TWT * (200 - dZ_1))$$

Here C_p =4178 J kg⁻¹ °C⁻¹, ρ_1 (1021.84 kg m⁻³) and ρ_2 (1023.64 kg m⁻³) are modern observed climatological mean potential densities of 0-70 m and 70-200 m (from the World Ocean Atlas 2013 [WOA13] datasets, version 2)⁶¹⁻⁶² for the nine cores (Extended Data Fig. 5a-b), while dZ₁ (the depth of D26) is determined by the vertical temperature gradient (Δ T) between SST and TWT, which exhibits a modern linear regression relationship (dZ₁=155.62-13.59× Δ T) in the Simple Ocean Data Assimilation (SODA) reanalysis dataset⁶³ over the years from 1871 to 2010 (Extended Data Fig. 5c-d). In this study, bottom depth of upper thermocline (the depth of 20°C isotherm, expressed as dZ₂) is simply fixed at 200 m, slightly deeper than

the maximum (188 m) of dZ_2 in Extended Data Fig. 5a. This simplification is adopted here to avoid uncertainties caused by calculating dZ_2 from proxy.

Note that we have also performed calculation based on a varying dZ_2 (defined by an extrapolative regression of SST and TWT), and the estimated OHC are similar to that of a fixed dZ_2 (at 200 m) but with smaller absolute value (because modern IPWP mean dZ_2 is only 160.5 m in Extended Data Fig. 5a). As an additional constraint, our proxy-reconstructed OHC averages 2.10×10^{10} J/m² during $0\sim3$ ka, which matches well with modern observed regionally averaged OHC over the IPWP (15° S- 15° N, 110° E- 160° W) above 200 m water depth (2.08×10^{10} J/m²). Another uncertainty may come from the glacial-interglacial changes of sea water density, but we argue that this effect on OHC can be neglected because OHC changes will be only 0.16% if considering a glacial density increase of 1.7 kg m⁻³ from modern 1021 kg m⁻³ for tropical surface oceans⁶⁴, rather smaller than the error range of our reconstructed OHC (1σ error 0.08×10^{10} J/m², equivalent to 3.8%, or 2σ error 0.11×10^{10} J/m², equivalent to 5.2%).

The seawater $\delta^{18}O$ ($\delta^{18}O_{sw}$) at each core is calculated from *G. ruber* ($\delta^{18}O_c$) by subtracting the effect of calcification temperature (estimated by Mg/Ca) using the transfer equation ($\delta^{18}O_{sw} = \delta^{18}O_c + (SST-16.5)/4.8 + 0.27$) according to Bemis et al⁶⁵ and by correcting for the effect of global ice volume changes ($\delta^{18}O_{ice}$) using the late Pleistocene global sea level stack (+1.17‰ for 130 meters' sea level drop)⁶⁶. Finally. the $\delta^{18}O_{sw}$ stack is calculated by compiling the $\delta^{18}O_{sw}$ of 10 cores, with a mean error of 0.16 ‰ (1 σ) or 0.31 ‰ (2 σ). Note that the non-linear relationships between ice-sheet and seawater $\delta^{18}O^{67}$ are not included here because such an effect results in little difference in our $\delta^{18}O_{sw}$ estimation over the last 360 ka when the Northern Hemisphere ice-sheet waxing and waning dominated global ocean $\delta^{18}O_{sw}$ change.

Spectral Analyses

All frequency spectrum analyses are performed by Redfit software⁶⁸ (window = rectangle,

segments = 4, oversample = 3 unless otherwise stated), and the spectral amplitudes are shown as the ratio relative to theoretical red noise (called Signal-to-Noise ratio, S/N ratio). But in Fig. 2f-h and Extended Data Fig. 7, both the original spectral amplitude and S/N ratio are given. Cross spectrum analyses are performed using the Analyseries software⁶⁹ with the B-Tukey method (window = Bartlett) to detect the phase angle and coherence of each time series relative to specific orbital variables (i.e., obliquity or precessional parameter⁷⁰).

Transient Model Simulations

We used the Community Earth System Model 1.0.4 (CESM)⁷¹ with T31_gx3v7 resolution (3.75°×3.75° and vertical 27 levels for atmosphere, nominal 3° resolution and vertical 60 levels for ocean) to simulate the annual mean OHC changes on orbital timescales. As a spin-up, the CESM was run for 200 model years under fixed orbital parameters⁷⁰ and greenhouse gases (GHG) of 300 kyr BP, with all other boundary conditions (but neglecting ice sheet changes) set for their values in 1950 AD. Then the model was integrated for 3000 model years with the transient orbital insolation forcing and GHG forcing of the last 300,000 years, in which orbital parameters and GHG were both advanced by 100 years at the end of each model year⁷². This transient experiment is called CESM_ghg and its outputs for the last 3000 model years are used in our analysis.

The simulated upper OHC (Joules m^{-2}) is calculated according to the following equation 73-74:

531
$$OHC = \int_{z}^{0} C_{p} * \rho * T * dz = C_{p} * \sum_{i=1}^{n} (\rho_{i} * T_{i} * dZ_{i})$$

Here C_p is the heat capacity of sea water taken as 4178 J kg⁻¹ °C⁻¹, ρ is potential density, T is ocean temperature, z is the depth of 20 °C isotherm (or D20) or a fixed water depth (i.e. 200 m), n is the total layers from surface to the depth z, and ρ_i , T_i , dZ_i are density, temperature, and layer thickness for the layer i. The annual mean OHC was regionally averaged over the

IPWP (15°S-15°N, 110°E-160°W, black rectangle in Fig. 1b), and its absolute value (1.43×10¹⁰ J/m²) during 0~3 ka is consistent with modern observed OHC above D20 (1.49×10¹⁰ J/m²) but smaller than the OHC above 200 m water depth (because of the shallower D20 than 200 m). The simulated OHC time series were 9-points smoothed and linearly detrended for better comparison with paleo-proxies.

We also performed transient experiments with a water isotope (δ¹⁸O)-enabled air-sea coupled climate model from the Goddard Institute for Space Studies of USA (GISS_ModelE2-R model)⁷⁵⁻⁷⁶ under same configurations of those in experiment CESM_ghg. Water isotope tracers (¹H₂¹⁶O, "normal" water; ²H₁H¹⁶O or HDO, reported as δD; and ¹H₂¹⁶O, δ¹ਐO) are incorporated into the atmosphere, land surface, sea ice, and ocean. Water isotopes are tracked through all stages of the hydrologic cycle and are advected throughout the model. At each phase change a fractionation is applied that explicitly determines equilibrium fractionation, with parameterizations accounting for kinetic fractionations during evaporation, condensation, evaporation of stratiform precipitating water droplets, and during condensing vapor to ice crystals in cloud under super-saturation conditions⁷⁷. This model has a horizontal resolution of 4° latitude ×5° longitude (both for the atmosphere and ocean), with 20 vertical layers in the atmosphere (up to 0.1 hPa) and 13 vertical layers in the Russell ocean model ⁷⁸⁻⁷⁹. This transient experiment is called GISS_ghg (also with spin-up of 200 model years) and its outputs for the last 3000 model years are used in our analysis.

As referred as $\delta^{18}O_{sw}$ _GISS and $\delta^{18}O_{p}$ _GISS (Fig. 3), the $\delta^{18}O$ of sea surface water ($\delta^{18}O_{sw}$) are regional averaged over the IPWP (5°S-15°N, 140°E-170°E), and the $\delta^{18}O$ of atmospheric precipitation ($\delta^{18}O_{p}$) were averaged over East Asia (15°N-40°N, 85°E-125°E), respectively (Supplementary Information Table 3). Regionally averaged time series are also calculated for other hydrological variables (i.e., precipitation, evaporation, precipitation minus evaporation, and evaporated water-vapor $\delta^{18}O$ [$\delta^{18}O_{evap}$]), shown in Extended Data Fig. 8. Note

that $\delta^{18}O_p$ or $\delta^{18}O_{evap}$ are calculated with precipitation or evaporation weights for each month before calculating their seasonal or annual means. According to atmospheric moisture balance equation⁸⁰, positive precipitation-minus-evaporation (or P-E) equals moisture convergence (or input moisture from outside), and thus negative values of P-E stand for local moisture divergence (or output moisture). Generally, atmospheric moisture is transported from negative P-E regions (as a source) toward positive P-E regions (as a sink), which means that P-E can be taken as a simple proxy of moisture source / sink pattern (but not the original source of evaporation).

Annual mean IPWP OHC above 20°C isotherm depth is calculated from GISS_ghg experiment using the same method as for CESM_ghg. Resulted OHC time series matches well with the results from CESM_ghg experiment (Extended Data Fig. 8e) but with smaller magnitudes, which may be attributed to the lower ocean resolution of GISS_ModelE2-R model (only 13 layers vertically) compared to that of CESM model (60 layers vertically). Thus, our interpretations regarding OHC rely on simulations of CESM_ghg.

Inter-model comparison and oceanic feedbacks

JAS averaged variables from our transient simulations (GISS_ghg and CESM_ghg) are used to illustrate the spatial patterns of precessional forced hydroclimatic changes. At P_{min} of the last 300,000 years, increased IPWP OHC is associated with paleo-ENSO-like and paleo-IOD-like air-sea coupled modes^{46, 81} (Extended Data Fig. 9), in the meanwhile, (1) SST increases more in the western parts of tropical Indian-Pacific Ocean with local low surface pressure anomalies, resulting in anomalous westward moisture transport from high pressure regions (the subtropical Pacific and central equatorial Pacific); (2) more moisture is converged upward and precipitated (with negative $\delta^{18}O_p$ anomalies) over the Indonesia, northern Indian Ocean, and African-Asian monsoon regions, but with drier conditions (moisture divergence and

positive $\delta^{18}O_p$ anomalies) over the tropical south Indian Ocean, central equatorial Pacific, and subtropical north and south Pacific oceans (Fig. 4e; Extended Data Fig. 9g-h); (3) evaporation decreases with more positive $\delta^{18}O$ ($\delta^{18}O_{evap}$) in the Indonesia and northern Indian Oceans, opposite to the anomalously increased evaporation with negative $\delta^{18}O_{evap}$ in the tropical south Indian ocean, central equatorial Pacific and subtropical Pacific oceans.

586

587

588

589

590

591

592

593

594

595

596

597

598

599

600

601

602

603

604

605

606

607

608

609

610

To verify the robustness of our transient simulations, we compared them with previous published model outputs from equilibrium experiments of the stable water isotope tracerenabled version of CESM (iCESM 1.2) 82 , in which the atmosphere is on a 1.9° latitude \times 2.5° longitude grid with 30 vertical levels and the ocean use a \sim 1° rotated pole grid, 60 vertical levels. Here we use the last 48 model years' result from two experiments (each 550 model years) with fixed precession parameter (P_{min} v.s. P_{max}) (Extended Data Fig. 9c), in which eccentricity is set as 0.0493 to maximize the influence of precession^{36, 83} (data available at http://doi.org/ 10.5281/zenodo.3354638). The differences of JAS precipitation, evaporation and moisture transport between P_{min} and P_{max} from iCESM (not shown) are generally similar to those from our transient experiments (GISS ghg; Extended Data Fig. 9), indicating that our results are reliable. Especially, regional averaged precipitation δ¹⁸O_p over East Asia (15°N-40°N, 85°E-125°E) in iCESM differs by -1.54‰ between P_{min} and P_{max}, which is much smaller than the difference of Chinese speleothem $\delta^{18}O$ (-3.86‰) between the P_{min} at 220 ka and the P_{max} at 209 ka (with similar eccentricity of 0.0493), and also smaller than the $\delta^{18}O_p$ difference in experiment GISS ghg (unsmoothed data: -6.83%, smoothed data: -3.36%), indicating a better performance of GISS model.

Similar equilibrium experiments are performed using the low-resolution version of CESM (T31_gx3v7) with different air-sea coupled configurations to isolate the role of oceanic feedbacks. The first group of experiments of P_{min} and P_{max} (using modern eccentricity value of 0.0167) are configured with fully dynamical ocean component and run for 300 model years,

while the other group experiments run 100 model years with a fixed modern SST to force the atmosphere⁸⁴. Based on the results of the last 50 model years, the differences between experiments of P_{min} and P_{max} are first calculated for the dynamical ocean coupled experiments (CESM-dyn-ocn) and the atmosphere alone experiments (CESM-atm-alone), respectively. Then the P_{min}-minus-P_{max} differences from these two experiment groups (i.e., CESM-dyn-ocn minus CESM-atm-alone) are compared to show the influence of dynamic oceanic feedbacks.

Generally, those JAS anomalies of surface pressure, 850 hPa wind, and moisture-source/sink in fully coupled experiments (CESM-dyn-ocn) exhibit similar patterns relative to those in Fig. 4d and Extended Data Fig. 9b, and they are also reproduced by CESM-atm-alone experiments (Extended Data Fig. 10a-b). This means that anomalous enhanced ocean-continent thermal contrast set the first-order responding features of Asian summer monsoon under precessional forcing⁸⁴. But the influence of oceanic feedbacks is also very clear, especially for the subtropical northwest Pacific and south Pacific High pressure and wind anomalies, and associated moisture transport from the Pacific to Indian Oceans (Extended Data Fig. 10c-d). Due to oceanic feedbacks, P_{min}-minus-P_{max} differences of the western Pacific subtropical High pressure, EASM southerly wind velocity and precipitation are furtherly amplified by another 1.16 hPa (over 30°N-50°N, 100°E-180°E), 1.36 m/s (over 30°N-50°N, 100°E-125°E), and 0.31 mm/day (over 15°N-40°N, 85°E-125°E) in CESM-dyn-ocn experiments, relative to 0.92 Pa, 0.46 m/s and 0.08 mm/day in CESM-atm-alone experiments.

This amplification effect is also reflected in those anomalous intensified moisture sources (divergence) in the southwest to eastern equatorial Indian Ocean, the central equatorial Pacific, and the subtropical Pacific Oceans (shown by box-averaged numbers in Extended Data Fig. 10b, d). Except for the western Indian Ocean, those stronger moisture sources are mainly contributed by reduced precipitation, because oceanic feedbacks only results in moderate increase of evaporation relative to precipitation changes (Extended Data Fig. 10e-f). Especially,

the two strongest moisture sources in the southeastern equatorial Indian and the central equatorial Pacific match well with anomalous downward branch of atmospheric Walker Circulation due to a combination of positive paleo-IOD and La Nina-like paleo-ENSO^{46, 84}.

Extended Data Fig. 10d exhibits anomalous increased moisture convergence (0.867 mm/day) in the Arab Sea, Bay of Bengal, and the South China Sea (5°N-25°N, 50°E-140°E), which convert the Asian marginal seas from anomalous moisture source (in CESM-atm-alone experiments) to moisture sink (in CESM-dyn-ocn experiments) of Asian summer monsoon. After excluding this potential moisture source, the intensified EASM moisture sink is largely contributed by the Pacific moisture sources, while the strongest moisture sinks in the western and north Indian Ocean (also the rising branch of positive IOD with increased precipitation) are dominated by moisture sources from the southwestern and eastern equatorial Indian Oceans (Extended Data Fig. 10).

Considering these independent responses of moisture transport in the Indian and Pacific Oceans, we argue for a critical role of the IPWP upper OHC on amplifying the EASM through paleo-ENSO-like air-sea coupled mode at the precessional band, which again calls for the atmospheric 'water tower' effect by converging remote Pacific moisture and transferring to boreal summer continental monsoon regions.

Modern Observation Analogs

The World Ocean Atlas 2013 (WOA13) datasets (version 2)⁶¹⁻⁶² are used to calculate annual mean climatological distributions of modern OHC above 200 m (Fig. 1a) according to the same equation as in CESM, and vertical profiles of IPWP ocean temperature / density at locations of the nine sediment cores (Extended Data Fig. 5).

As a central part of the energetic recharge-discharge process in tropical oceans, modern IPWP OHC can greatly influence Asian-Indo-Pacific monsoonal precipitation (through ENSO,

IOD and tropical cyclones)⁶. Here we use the same equation as in the CESM to calculate annual mean OHC above 200 m or the depth of 20 °C isotherm from the year 1871 to 2010 based on the SODA reanalysis dataset (version 2.2.4)⁶³. Then we investigate the ENSO-related linkage between OHC and δ^{18} O_p changes by comparing with annual mean outputs from the historical nudged simulation (1970-2008) of the atmospheric component of GISS_ModelE2-R, which participated in the Stable Water Isotope Intercomparison Group, phase 2 (SWING2)⁸⁵.

Regional averaged OHC time series over IPWP (15°S-15°N, 110°E-160°W) are compared with global averaged SST anomaly (SSTA) of the annual mean Extended reconstructed SST (ERSST. V4)⁸⁶, the Southern Oscillation Index (SOI) from the Climatic Research Unit (https://crudata.uea.ac.uk/cru/data/soi/)⁸⁷, and those time series of East Asian precipitation and associated $\delta^{18}O_p$ averaged over 15°N-40°N and 85°E-125°E. Regression coefficients of OHC, $\delta^{18}O_p$ and precipitation against the normalized time series of SOI are also calculated over the years of 1970~2008 (shown in Fig. 1b-c and Extended Data Fig. 1).

- Data availability: All data are presented in the main text or supplementary materials.
- Meanwhile, data reported here are also stored in the Pangaea database (www.pangaea.de).

- Code availability: Codes for GISS ModelE2-R (version modelE2 AR branch.2017.11.02
- 679 07.50.01) and CESM (version 1.0.4) are publicly available at https://simplex.giss.nasa.gov/
- snapshots/ and https://www.cesm.ucar.edu/models/cesm1.0/, respectively. Model outputs were
- 681 processed using the NCAR Command Language (NCL, version 6.6.2, available at
- 682 https://www.ncl.ucar.edu) and plotted using the Grid Analysis and Display System (GrADS,
- version 2.0.2, available at http://www.iges.org/grads/grads.html).

- 48. Lea, D. W., Pak, D. K. & Spero, H. J. Climate impact of late Quaternary equatorial Pacific sea surface
- temperature variations. *Science* **289**, 1719-1724 (2000).

- 687 49. Lisiecki, L. E. & Raymo, M. E. A Pliocene-Pleistocene stack of 57 globally distributed benthic δ¹⁸O
- records. *Paleoceanography* **20**, PA1003 (2005).
- 689 50. Bolliet, T. et al. Mindanao Dome variability over the last 160 kyr: Episodic glacial cooling of the West
- 690 Pacific Warm Pool. *Paleoceanography* **26**, PA1208 (2011).
- 691 51. Holbourn, A., Kuhnt, W. & Xu, J. Indonesian Throughflow variability during the last 140 ka: the Timor
- 692 Sea outflow. *Geol. Soc. Spec. Publ.* **355**, 283-303 (2011).
- 52. Zhang, J. et al. Western equatorial Pacific productivity and carbonate dissolution over the last 550 kyr:
- 694 Foraminiferal and nannofossil evidence from ODP Hole 807A. Mar. Micropaleontol. 64, 121-140
- 695 (2007).
- 696 53. Dang, H., Jian, Z., Kissel, C. & Bassinot, F. Precessional changes in the western equatorial Pacific
- 697 hydroclimate: A 240 kyr marine record from the Halmahera Sea, East Indonesia. *Geochem. Geophys.*
- 698 *Geosyst.* **16**, 148-164 (2015).
- 699 54. Dang, H., et al. Precession insolation and sea level changes regulate the iron-associated sediment
- supplies from Papua New Guinea to the equatorial Pacific. *Quat. Sci. Rev.* **239**, 106361 (2020).
- 701 55. Holbourn, A. et al. Orbitally paced paleoproductivity variations in the Timor Sea and Indonesian
- Throughflow variability during the last 460 kyr. *Paleoceanography* **20**, PA3002 (2005).
- 703 56. Visser, K., Thunell, R. & Goñi, M. A. Glacial-interglacial organic carbon record from the Makassar
- Strait, Indonesia: implications for regional changes in continental vegetation. *Quat. Sci. Rev.* **23**, 17-27
- 705 (2004).
- 706 57. Xu, J., Holbourn, A., Kuhnt, W., Jian, Z., & Kawamura, H. Centennial changes in the thermocline
- structure of the Indonesian Outflow during Terminations I and II. Earth Planet. Sci. Lett. 273, 152-162
- 708 (2008).
- 709 58. Zuraida, R. et al. Evidence for Indonesian Throughflow slow-down during Heinrich Events 3-5.
- 710 *Paleoceanography* **24**, PA2205 (2009).
- 711 59. Anand, P., Elderfield, H. & Conte, M. H. Calibration of Mg/Ca thermometry in planktonic foraminifera
- from a sediment trap time series. *Paleoceanography* **18(2)**, 1050 (2003).
- 713 60. Mohtadi, M. et al. North Atlantic forcing of tropical Indian Ocean climate. *Nature* **509**, 76-80 (2014).
- 714 61. Locarnini, R.A. et al. and others. World Ocean Atlas (2013) version 2 (WOA13 V2), Volume 1:
- 715 Temperature. In: NOAA National Centers for Environmental Information S. Levitus, ed, and A.

- Mishonov, technical ed, NOAA Atlas NESDIS 73, NOAA National Centers for Environmental
- 717 Information, Silver Spring, Maryland, pp 40. (2013).
- 718 62. Zweng, M. M. et al. and others. World Ocean Atlas (2013) version 2 (WOA13 V2), Volume 2: Salinity.
- In: NOAA National Centers for Environmental Information, S. Levitus, ed, and A. Mishonov, technical
- ed, NOAA Atlas NESDIS 74, NOAA National Centers for Environmental Information, Silver Spring,
- 721 Maryland, pp 39. (2013).
- 722 63. Carton, J. A. & Giese, B. S. A reanalysis of ocean climate using Simple Ocean Data Assimilation 425
- 723 (SODA). Mon. Weather Rev. **136**, 2999-3017 (2008).
- 724 64. Billups, K. & Schrag, D. Surface ocean density gradients during the Last Glacial Maximum.
- 725 *Paleoceanography* **15**. 110-123 (2000).
- 726 65. Bemis, B. E., Spero, H. J., Bijma, J. & Lea, D. W. Reevaluation of the oxygen isotopic composition of
- 727 planktonic foraminifera: Experimental results and revised paleotemperature equations.
- 728 *Paleoceanography* **13(2)**, 150-160 (1998).
- 729 66. Spratt, R. M. & Lisiecki, L. E. A Late Pleistocene sea level stack. *Clim. Past* **12**, 1079-1092 (2016).
- 730 67. Rohling, E. J., Yu, J., Heslop, D., Foster, G. L., Opdyke, B. & Roberts, A. P. Sea level and deep-sea
- temperature reconstructions suggest quasi-stable states and critical transitions over the past 40 million
- 732 years. *Sci. Adv.* **7(26)**, eabf5326 (2021).
- 733 68. Schulz, M. & Mudelsee, M. REDFIT: estimating red-noise spectra directly from unevenly spaced
- paleoclimatic time series. *Comput. Geosci.* **28**, 421-426 (2002).
- 735 69. Paillard, D., Labeyrie, L. & Yiou, P. Macintosh program performs time-series analysis. *Eos Trans. AGU*
- 736 77, 379-379 (1996).
- 737 70. Laskar, J. et al. A long term numerical solution for the insolation quantities of the Earth. Astron.
- 738 *Astrophys.* **428**, 261-285 (2004).
- 739 71. Shields, C. A. et al. The low-resolution CCSM4. *J. Clim.* **25**, 3993-4014 (2012).
- 740 72. Kutzbach, J. E., Liu, X. D., Liu, Z. Y. & Chen, G. S. Simulation of the evolutionary response of global
- summer monsoons to orbital forcing over the past 280,000 years. Clim. Dynam. 30(6), 567-579 (2008).
- 742 73. Pu, S. Z., Yu, F., Hu, X. M. & Chen, X. R. Spatial and temporal variability of heat content above the
- thermocline in the tropical Pacific Ocean. *Acta Oceanol. Sin.* **22(2)**, 179-190 (2003).
- 74. Yang, X. X., Wu, X. F., Liu, Z. H. & Yuan, C. X. A preliminary study on an upper ocean heat and salt

- 745 content of the western Pacific warm pool region. *Acta Oceanol. Sin.* **38**, 60-71 (2019).
- 746 75. Schmidt, G. A. et al. Configuration and assessment of the GISS ModelE2 contributions to the CMIP5
- 747 archive. J. Adv. Model. Earth Syst. 6, 141-184 (2014).
- 748 76. Lewis, S. C., LeGrande, A. N., Schmidt, G. A. & Kelley, M. Comparison of forced ENSO-like
- hydrological expressions in simulations of the preindustrial and mid-Holocene. J. Geophys. Res. Atmos.
- 750 **119(12)**, 7064-7082 (2014).
- 751 77. Schmidt, G. A., Hoffmann, G., Shindell, D. T. & Hu, Y. Modeling atmospheric stable water isotopes and
- the potential for constraining cloud processes and stratosphere-troposphere water exchange. *J. Geophys.*
- 753 Res. Atmos. 110, 021314 (2005).
- 754 78. Russell, G. L., Miller, J. R. & Rind, D. A coupled atmosphere-ocean model for transient climate change.
- 755 Atmos. Ocean **33**, 683-730 (1995).
- 756 79. Russell, G. L., Miller, J. R., Rind, D. H., Ruedy, R. A., Schmidt, G. A. & Sheth, S. Comparison of model
- and observed regional temperature changes during the past 40 years. *J. Geophys. Res.* **105**, 14891-14898
- 758 (2000).
- 759 80. Trenberth, K. E. & Fasullo, J. T. Regional energy and water cycles: transports from ocean to land. J.
- 760 *Clim.* **26**(20), 7837-7851 (2013).
- 761 81. Wang, Y., Jian, Z., Zhao, P., Chen, J. & Xiao, D. Precessional forced evolution of the Indian Ocean
- 762 Dipole. J. Geophys. Res. Ocean **120(5)**, 3747-3760 (2015).
- Ready, E. et al. The connected isotopic water cycle in the Community Earth System Model version 1. J.
- 764 *Adv. Model. Earth Syst.* **11**, 2547-2566 (2019).
- 765 83. Tabor, C. R. et al. Interpreting precession-driven δ^{18} O variability in the South Asian monsoon region. J.
- 766 Geophys. Res. Atmos. 123, 5927-5946 (2018).
- 767 84. Wang, Y., Jian, Z., Zhao, P., Xiao, D. & Chen, J. Relative roles of land- and ocean-atmosphere
- interactions in Asian-Pacific thermal contrast variability at the precessional band. Sci. Rep. 6(1), 28349-
- 769 28349 (2016).
- Risi, C. et al. Process-evaluation of tropospheric humidity simulated by general circulation models using
- water vapor isotopologues: 1. Comparison between models and observations, *J. Geophys. Res. Atmos.*
- 772 **117**, D05303 (2012).
- 773 86. Huang, B. et al. Extended Reconstructed Sea Surface Temperature version 4 (ERSST.v4): Part I.

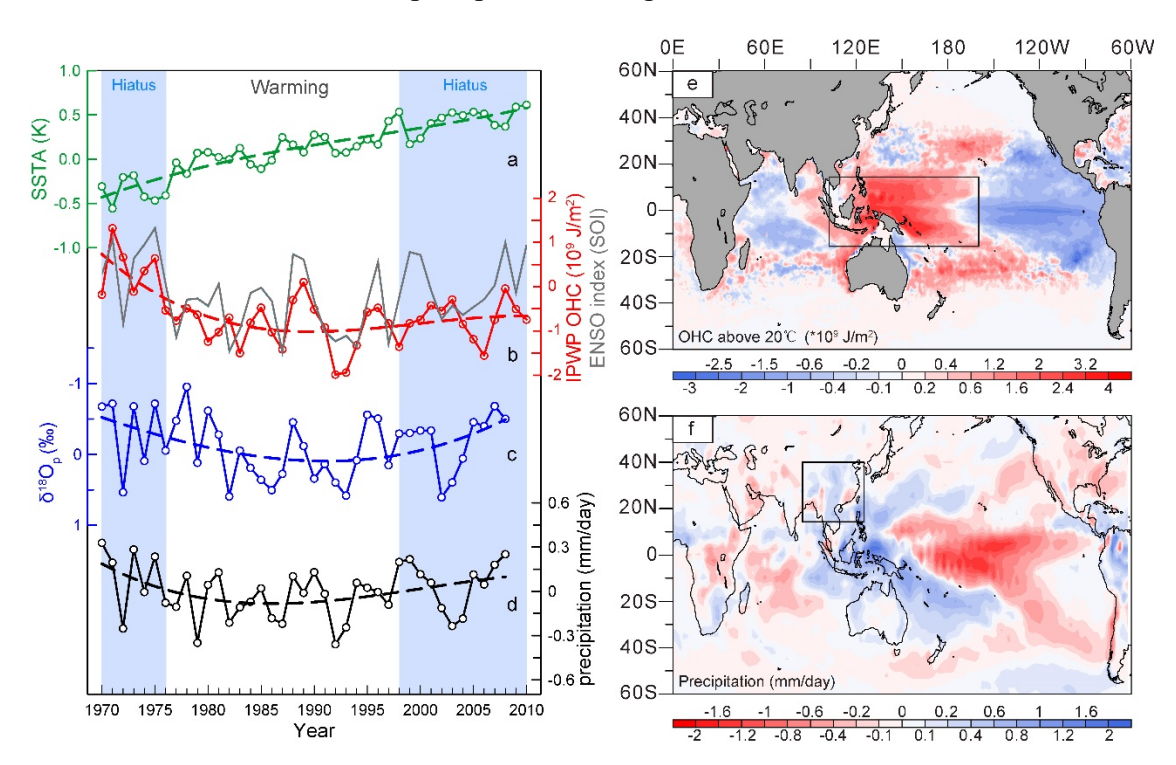
774 Upgrades and intercomparisons. J. Clim. 28, 911-930 (2014). 775 87. Ropelewski, C.F. & Jones, P. D. An extension of the Tahiti-Darwin Southern Oscillation Index. Mon. 776 Weather Rev. 115, 2161-2165 (1987). 777 778 **ACKNOWLEDGMENTS** 779 This work was supported by the National Natural Science Foundation of China (grants 42188102, 91958208 and 41976047). For this research, we used samples provided by the 780 781 cruises of Ocean Drilling Program, French R/V Marion Dufresne, German R/V Sonne and 782 Chinese R/V Kexue-1. We thank Peijun Qiao, Xinrong Cheng, Xiaoying Jiang, LiLing Hamady, 783 Dotti Pak, Georges Paradis, Tom Guilderson and Chao Zhou for lab support, and three 784 anonymous reviewers for their constructive suggestions. 785 786 Author contributions: Z.J. designed the research; Y.W. run the numerical simulation; Z.J., 787 H.D. and D.W.L. took the lead in the experiments, assisted by H.J., L.Y. and X.W.; M.M., Y.R., 788 D.W.L., Z.L. and W.K. helped with the interpretation; Z.J., Y.W. and H.D. wrote the first draft, 789 and all authors discussed and commented on the results and the manuscript. 790 791 **Competing interests:** The authors declare no competing interests. 792 793 **Additional information** 794 **Supplementary information** The online version contains supplementary materials available 795 at https://doi.org/10.1038/.....

Correspondence and requests for materials should be addressed to Z.J. or Y.W. or H.D.

796

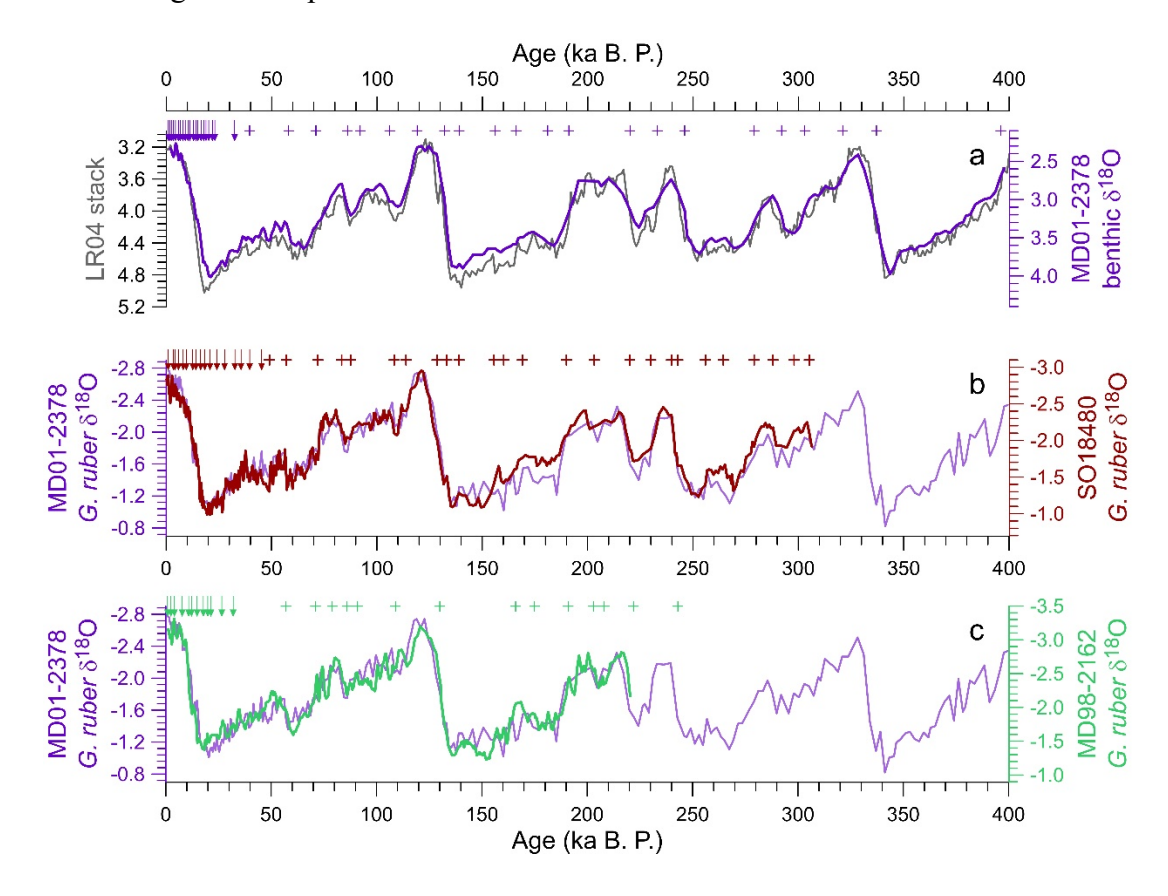
Extended Data Fig. 1 | Relations of precipitation and $\delta^{18}O_p$ in East Asia with SST and upper OHC of the IPWP over 1970-2010.

(a) Sea surface temperature anomaly (SSTA) of the annual mean ERSST (V4)⁸⁶. (b) annual mean OHC anomaly above 20 °C isotherm depth over IPWP (15°S-15°N, 110°E-160°W), calculated from the SODA reanalysis dataset. (c, d) annual mean anomalies of East Asian precipitation (black, d) and associated $\delta^{18}O_p$ (blue, c) (15°N-40°N, 85°E-125°E), based on the historical nudged simulation of the atmospheric component of GISS_ModelE2-R. Time series in (a-d) are calculated by subtracting the temporal average of each variable. Vertical bars indicate the major periods of global warming hiatus. Dashed thick lines are long term trends of 3-order polynomial fitting. (e) modern La Niña-associated annual mean OHC anomalies above 20 °C isotherm depth from SODA dataset, shown as regression coefficients against normalized time series of Southern Oscillation Index (SOI, gray line in (b)). (f) is the same as (e) but for La Niña-associated annual mean precipitation changes from the GISS historical simulation.



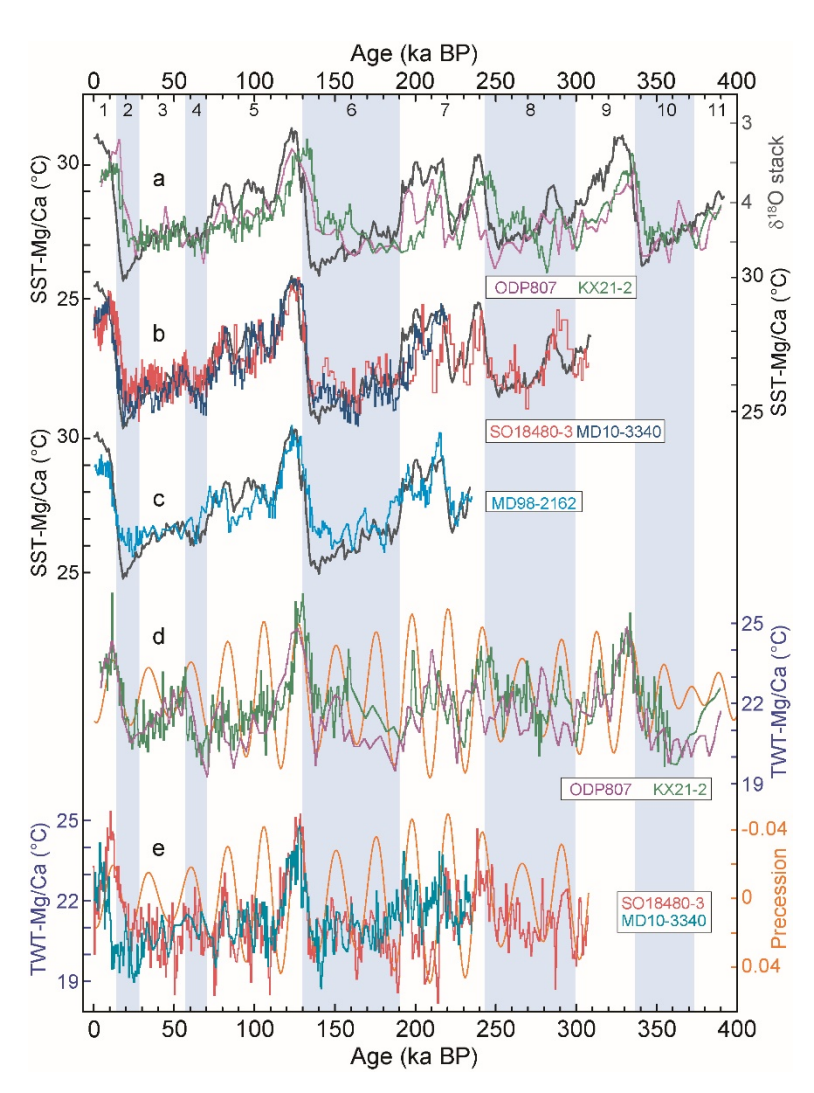
Extended Data Fig. 2 | Age models of cores SO18480-3 and MD98-2162.

(a) the age-model of a nearby core MD01-2378 based on its benthic foraminifera $\delta^{18}O$ correlated to the global stacked benthic foraminifera $\delta^{18}O$ (LR04 stack). (b, c) Comparisons of the *G. ruber* $\delta^{18}O$ of cores SO18480-3 (b) and MD98-2162 (c) to core MD01-2378. Arrows mark the AMS ^{14}C dates performed on planktic foraminifera *G. ruber*, while crosses mark the $\delta^{18}O$ -derived age control points.



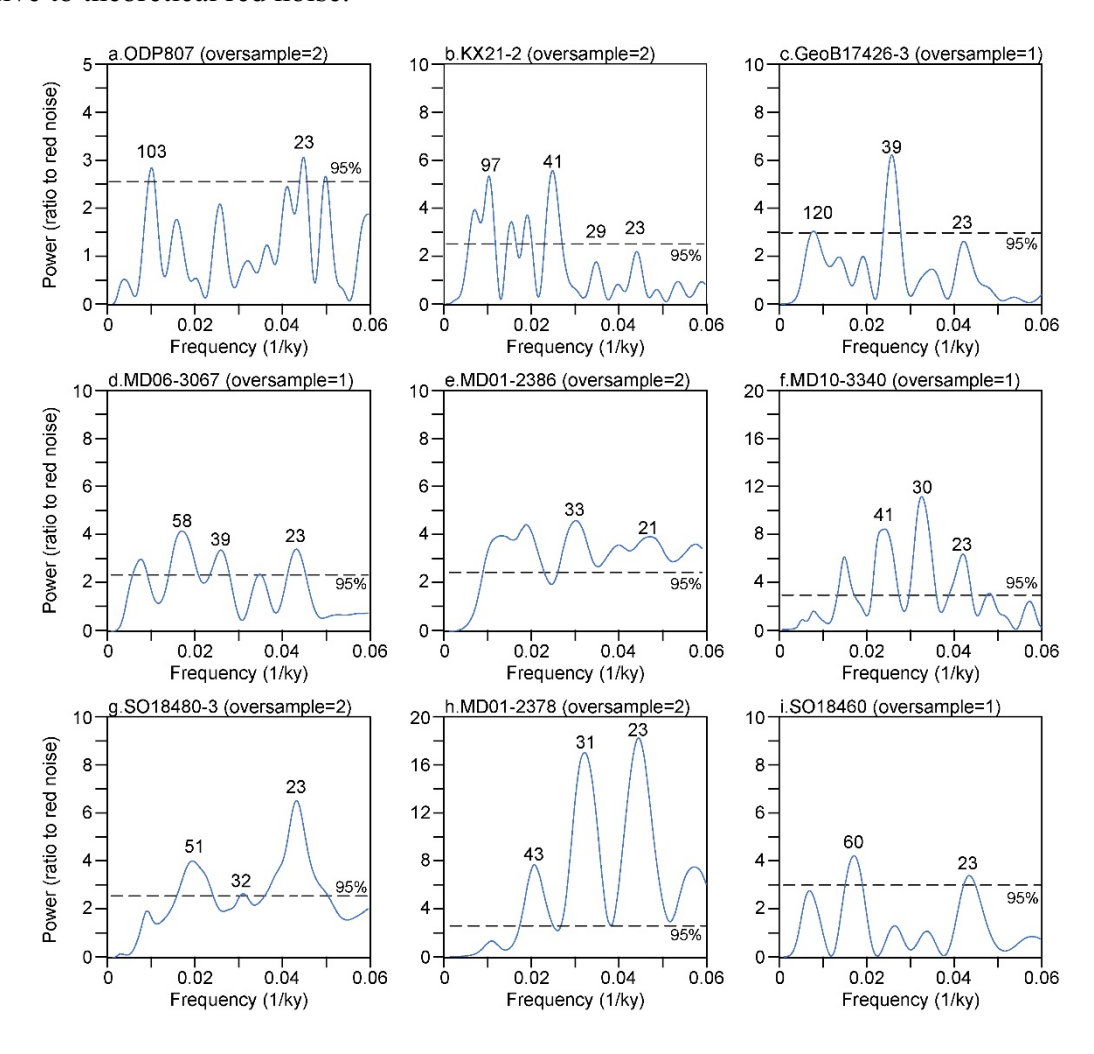
Extended Data Fig. 3 | Time series of original SSTs and TWTs.

(a) SSTs for core ODP807 (purple) and KX21-2 (green), (b) SSTs for MD10-3340 (blue) and SO18480-3 (red), (c) SST for MD01-2162 (dark blue), (d) TWTs for core ODP807 (purple) and KX21-2 (green), (e) TWTs for MD10-3340 (blue) and SO18480-3 (red). The global stacked benthic foraminifera δ^{18} O record (LR04 δ^{18} O_{benthic}) and precession parameter are also given in (a-c) and in (d-e) for comparison, respectively. Vertical bars indicate glacial marine isotope stages.



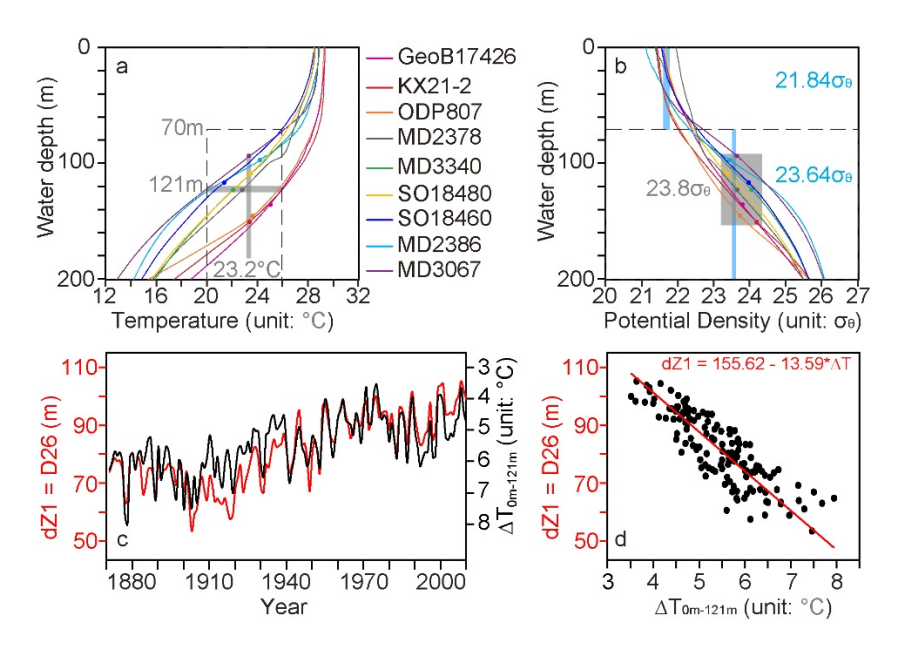
Extended Data Fig. 4 | Spectral amplitudes of original TWT time series.

(a) ODP807, (b) KX21-2, (c) GeoB17426-3, (d) MD06-3067, (e) MD01-2386, (f) MD10-3340, (g) SO18480-3, (h) MD01-2378, (i) SO18460. The spectral amplitudes, calculated by the Redfit software (window = rectangle, segments = 9, oversample = 2 or 1), are shown as the ratio relative to theoretical red noise.



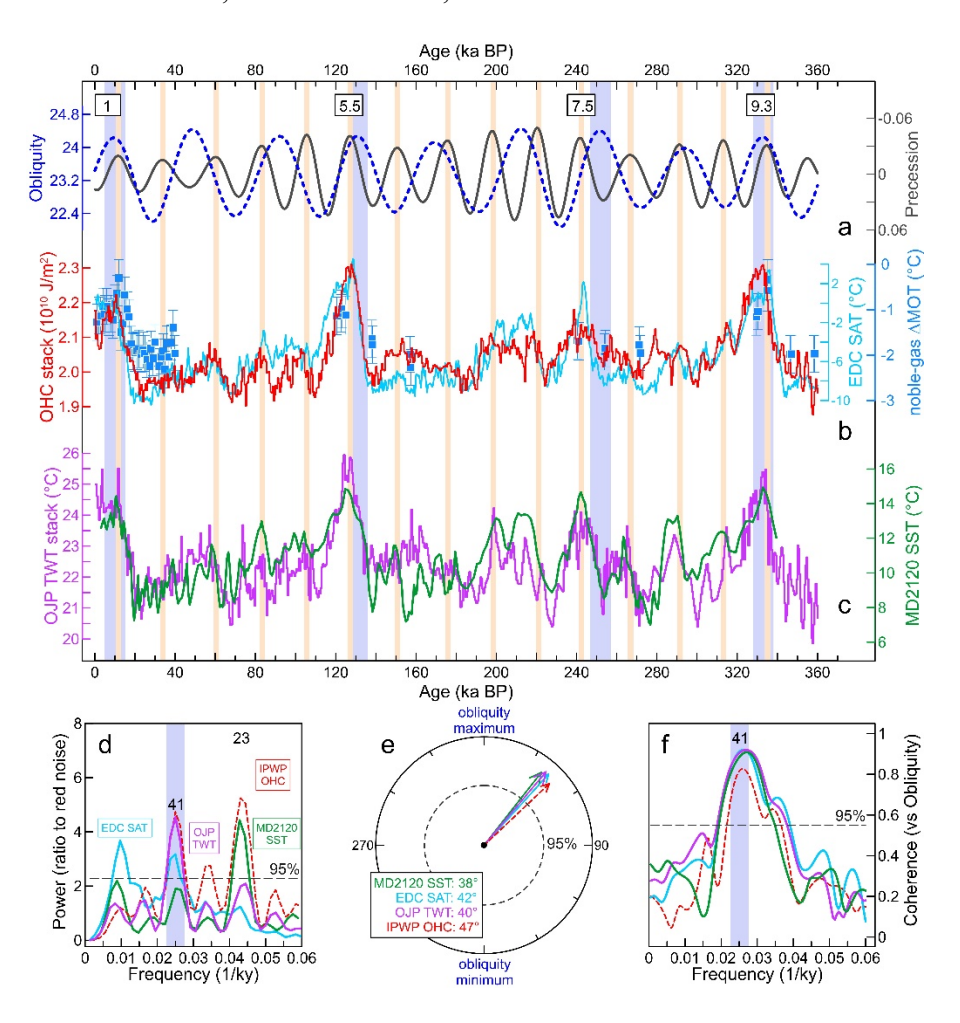
Extended Data Fig. 5 | Modern observational constraints for proxy-based OHC calculation.

(a) Climatological vertical profiles of annual mean temperature from WOA13 (colored lines) at locations of the nine sediment cores with paired SST and TWT records. Color filled dots mark the habitat depth of *P. obliquiloculata* for each core according to Mg/Ca-derived TWT averaged during the early-middle Holocene (6-10 ka), with a mean depth of 121 m and mean TWT of 23.2 °C (grey bars). Vertical dashed lines in (a) show the 20 °C and 26 °C isotherms, which range from ~70 to ~122 m and from ~110 to ~188 m in the IPWP (15°S-15°N, 110°E-160°W), respectively. (b) is similar to (a) but for potential density (colored lines and dots), with an average of 23.8 σ_0 at the habitat depth of *P. obliquiloculata*. According to the shallowest 26 °C isotherm depth of these nine cores, dashed line in (b) marks the boundary between the mixed layer (0-70 m, mean density=21.84 σ_0) and the upper thermocline layer (70-200 m, mean density=23.64 σ_0). (c) Time series of the 26 °C isotherm depth (D26) and vertical temperature gradient between 0 m and 121 m ($\Delta T_{0m-121m}$), calculated by averaging over the IPWP from SODA reanalysis dataset. (d) Linear regression relationship between D26 and $\Delta T_{0m-121m}$ (r = -0.85), that is used for assessing past changes of IPWP D26 from those of palaeoceanographic proxy-based ΔT ($\Delta T = SST - TWT$).



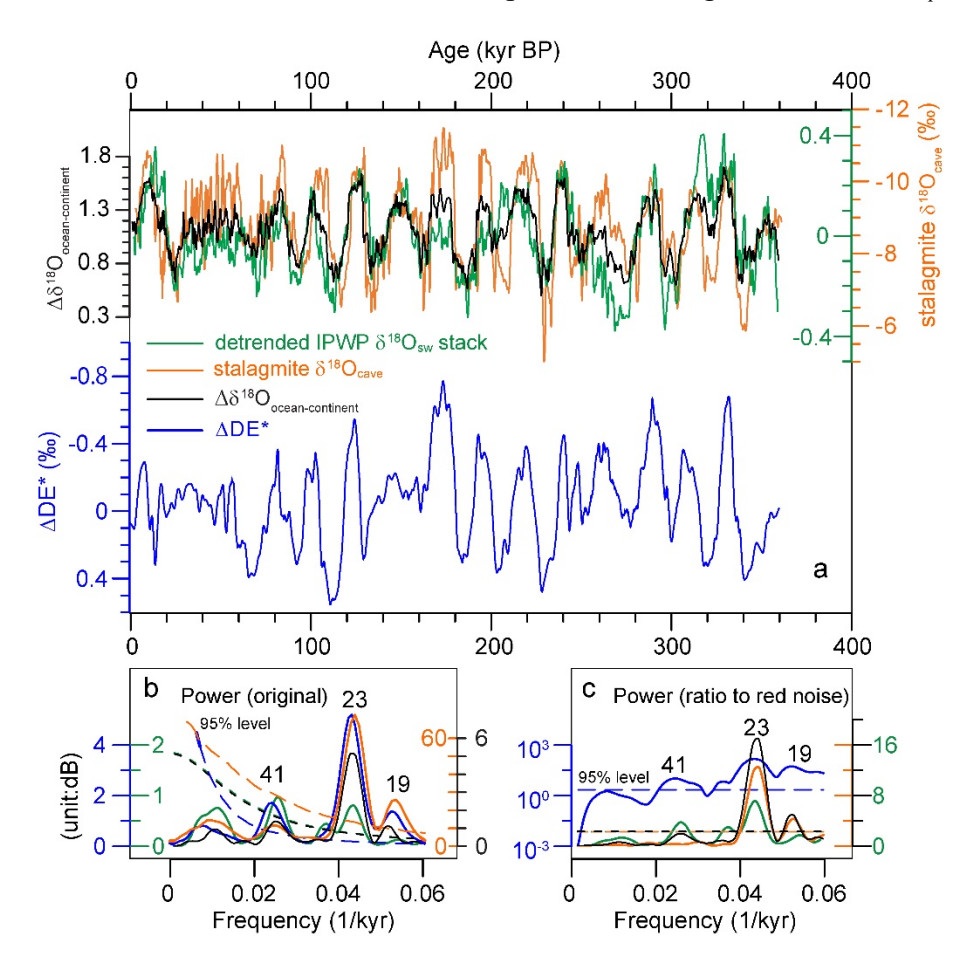
Extended Data Fig. 6 | Obliquity cycles in the IPWP upper OHC and Southern Hemisphere paleoclimate records.

(a) the obliquity (blue) and precessional parameters (gray). (b) IPWP OHC stack anomaly (red), compared with the surface air temperature from Antarctic EPICA Dome C ice core (EDC SAT; ice blue) and EDC noble-gas reconstructed global mean ocean temperature anomalies (ΔΜΟΤ, blue squares with vertical bars showing the error)⁸⁻⁹. (c) TWT stack of the Ontong Java Plateau sites (OJP, based on cores KX21-2 and GeoB17426, purple) and the Mg/Ca-SST record of the extratropical Southwest Pacific core MD97-2120 (MD2120 SST, green). In (a)-(c), the P_{min} and obliquity maxima are shown in brown and light purple vertical bars, respectively. (d)-(f) are similar to those in Fig. 3 but for the spectral/cross spectral (relative to the obliquity maxima) results of IPWP OHC stack, OJP TWT stack, EDC SAT and MD2120 SST.



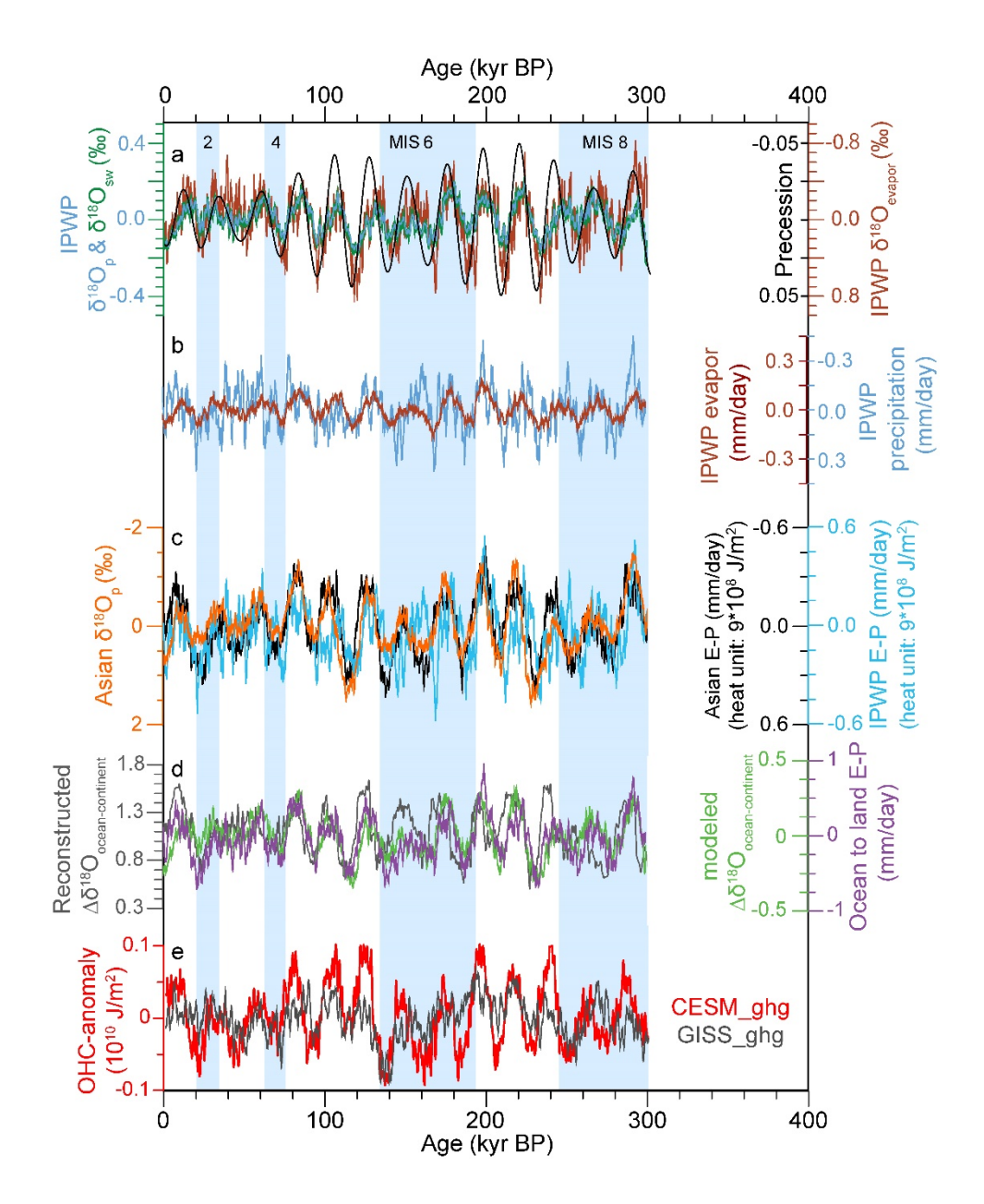
Extended Data Fig. 7 | δ^{18} O signatures of low-latitude hydrological cycle from the IPWP to Asian continent.

(a) the IPWP $\delta^{18}O_{sw}$ stack (green, detrended), Chinese speleothem $\delta^{18}O_{cave}$ (orange) and their differences ($\Delta\delta^{18}O_{ocean\text{-continent}}$, black), in comparison with another measurement of the low-latitude hydrological cycle (namely, the Dole Effect, ΔDE^* , blue). (b, c) spectral powers of these time series (solid lines) shown as original spectral amplitude (b) and the ratio relative to theoretical red noise (c), while dashed lines denote their 95 % confidence levels. Note that for calculating $\Delta\delta^{18}O_{ocean\text{-continent}}$, the $\delta^{18}O_{cave}$ is divided by a ratio of 7.85 according to the standard deviations of detrended $\delta^{18}O_{sw}$ (0.154) and $\delta^{18}O_{cave}$ (1.209), which is assumed to stands for the ocean-continent $\delta^{18}O$ fraction effect that will amplifies the changes in Asian $\delta^{18}O_p$.



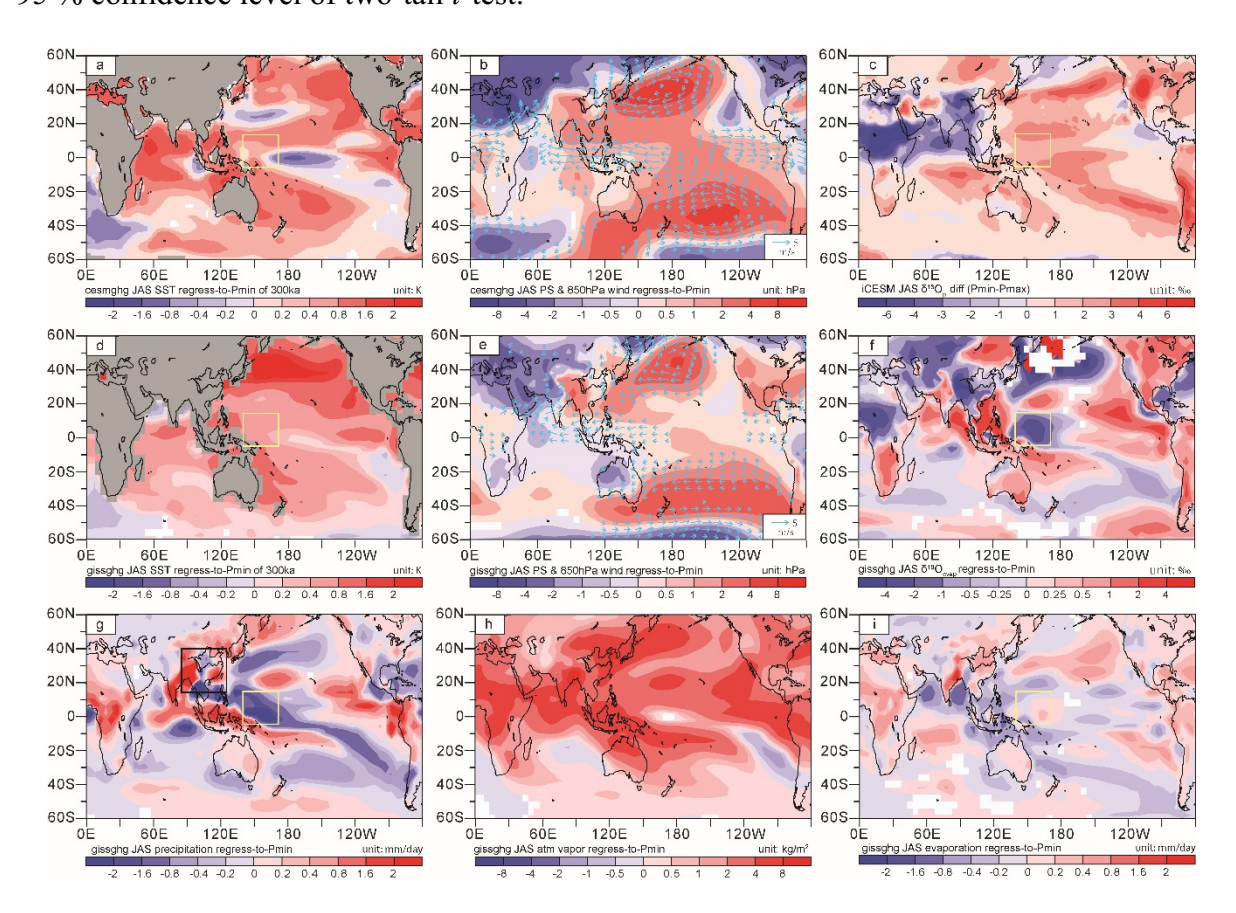
Extended Data Fig. 8 | Time series of hydroclimate indices of GISS ghg experiment.

(a) regional averaged $\delta^{18}O_{sw}$ (green), $\delta^{18}O_p$ (blue) and evaporated water vapor $\delta^{18}O_{evapor}$ (brown) over IPWP (5°S-15°N, 140°E-170°E). (b) similar to (a) but for the evaporation (brown) and precipitation (blue) rates over the IPWP. (c) regional averaged $\delta^{18}O_p$ (orange) and local hydrological balance (Evaporation minus Precipitation, E-P, black) over East Asian (15°N-40°N, 85°E-125°E), which are out-of-phase with the IPWP E-P (sapphire blue). The unit of mm/day can be converted to latent heat by multiplying 9×10^8 J/m² (\approx latent heat of precipitation at 0 °C: 2.5×10^6 J/kg by 360 days). (d) Differences of hydrological balance (E-P, purple) and $\delta^{18}O$ ($\Delta\delta^{18}O_{ocean-continent}$, green) between IPWP and East Asia in the GISS simulation, in comparison with the proxy-reconstructed $\Delta\delta^{18}O_{ocean-continent}$ (grey). (e) OHC above 20 °C isothermal depth from experiments CESM_ghg (red) and GISS_ghg (dark gray). All the GISS simulated time series are linearly detrended and 9-point or 18-point (only in b) smoothed. To calculate modeled $\Delta\delta^{18}O_{ocean-continent}$, the Asian $\delta^{18}O_p$ is divided by a ratio of 7.5 according to standard deviations of detrended IPWP $\delta^{18}O_{sw}$ (0.076) and Asian $\delta^{18}O_p$ (0.569) in a similar rationale as shown in Extended Data Fig. 7.



Extended Data Fig. 9 | Multi-model comparison of the spatial patterns of precession-forced changes in different hydroclimate indices.

(a-b) boreal summer (JAS) SST (shading), air pressure at surface (PS, shading) & 850 hPa wind (vector) anomalies at P_{min} from transient experiment CESM_ghg. (c) JAS $\delta^{18}O_p$ differences between P_{min} and P_{max} from two equilibrium experiments of iCESM (P_{min} minus P_{max}). (d-i) outputs from transient experiment GISS_ghg, including JAS SST (d), PS & 850 hPa wind (e), evaporated vapor $\delta^{18}O$ ($\delta^{18}O_{evap}$) (f), precipitation (g), vertical integrated atmospheric vapor content (h), and evaporation (i). Except for (c), white shading denotes areas not significant at 95 % confidence level of two-tail *t*-test. These patterns are shown as regression coefficients against the normalized time series of precession parameter, which are multiplied by -1 to demonstrate the effect of P_{min} relative to P_{max} . White shading denotes areas not significant at 95 % confidence level of two-tail *t*-test.



Extended Data Fig. 10 | Contributions of the oceanic feedbacks to precession-forced ocean-continent moisture transport.

912

913

914

915

916

917

918

919

920

921

922

923

924

925

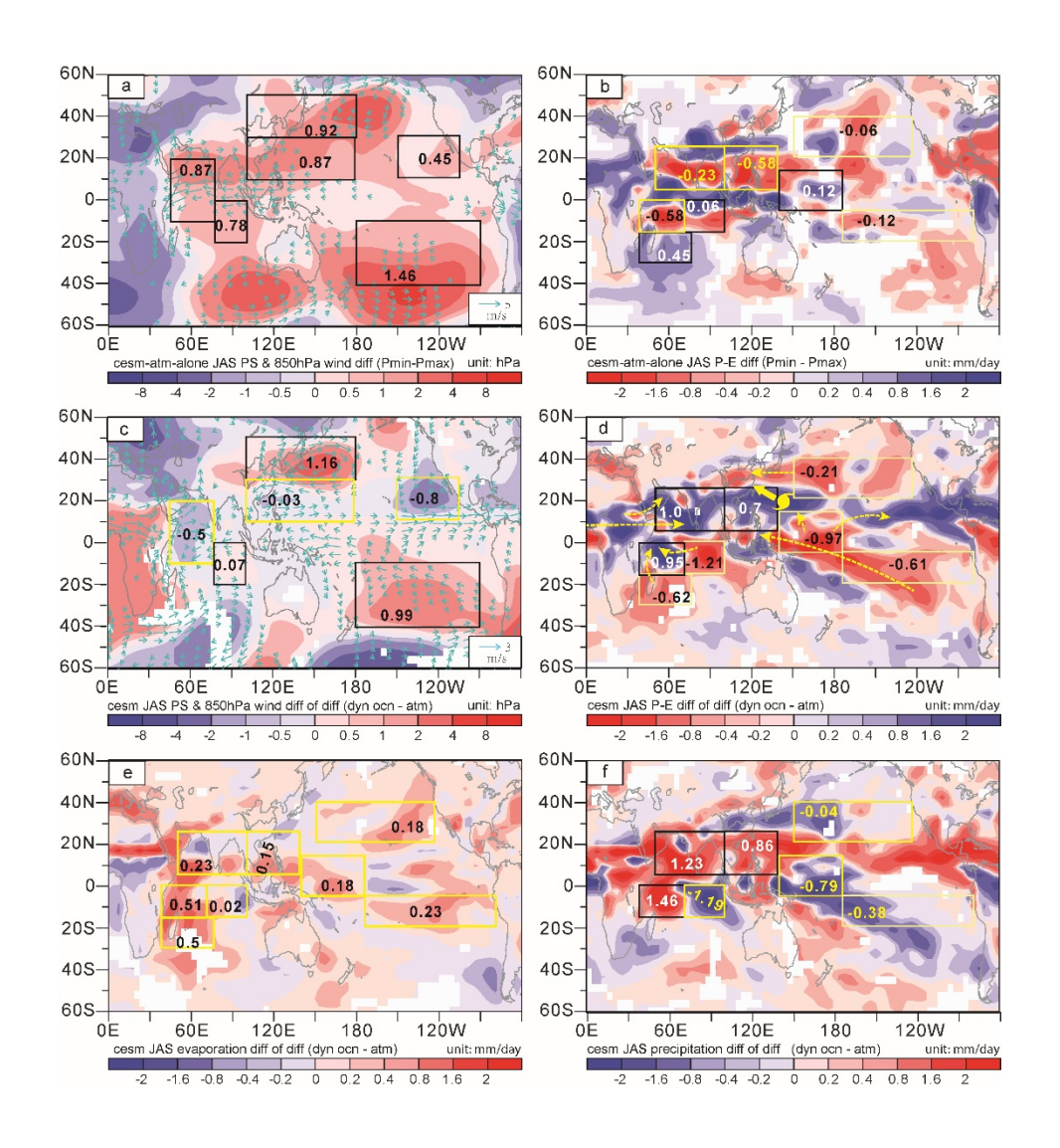
926

927

928

929

(a) boreal summer (JAS) air pressure at surface (PS) and 850 hPa wind differences between P_{min} and P_{max} from decoupled experiments with fixed modern SST (CESM-atm-alone experiments). (b) the same as (a) but for differences of atmospheric moisture transport flux divergence (indicated by P-E, negative values stand for moisture source). Variables in (c) and (d) are the same as (a) and (b), respectively, but for differences of the P_{min}-minus-P_{max} differences (or experiments CESM-dyn-ocn minus CESM-atm-alone), highlighting the role of OHC associated oceanic feedbacks. (e) and (f) are similar to (c) but for evaporation and precipitation, respectively. Yellow and black boxes in (a, c) are defined by negative and positive anomalies of surface air pressure in (c), respectively, and box averaged values are shown as numbers to quantify the role of oceanic feedbacks. Similarly, those boxes in (b, d-f) are defined by centers of anomalous atmospheric moisture transport flux divergences in (d) (yellow for source and black for sink). Yellow arrows and symbol in (d) show the schematic pathways of anomalous moisture transport from source to sink regions due to oceanic feedbacks, including the mean circulation sketched from vectors in (c) and contribution of tropical cyclones (similar to Fig. 4e). White shading denotes areas not significant at 95 % confidence level of two-tail ttest.



932 **Supplementary information** 933 934 Warm pool ocean heat content regulates ocean-continent moisture transport 935 936 Zhimin Jian^{1,*}, Yue Wang^{1,*}, Haowen Dang^{1,*}, Mahyar Mohtadi², Yair Rosenthal³, David W. 937 938 Lea⁴, Zhongfang Liu¹, Haiyan Jin¹, Liming Ye⁵, Wolfgang Kuhnt⁶, Xingxing Wang¹ 939 940 ¹State Key Laboratory of Marine Geology, Tongji University, Shanghai 200092, China. ²MARUM-Center for 941 Marine Environmental Sciences, University of Bremen, 28359 Bremen, Germany. 3Department of Marine and 942 Coastal Science and Department of Earth and Planetary Sciences, Rutgers University, New Brunswick, NJ 08901, 943 USA. ⁴Department of Earth Science, University of California, Santa Barbara, CA 93106, USA. ⁵Second Institute 944 of Oceanography, Ministry of Natural Resource, Hangzhou 310012, China. 6Institute of Geosciences, Christian-945 Albrechts-University, D-24118 Kiel, Germany. 946 947 * Correspondence to Z.J. (jian@tongji.edu.cn), Y.W. (163wangyue@163.com) or H.D. (hwdang@tongji.edu.cn) 948 949 950 **Contents** 951 Supplementary Table 1. Information of cores studied and cited in this work. 952 Supplementary Table 2. Data of the Mg/Ca-derived temperature estimates, age control points and the planktic δ^{18} O of cores ODP807, KX21-2, MD10-3340, SO18480-3 and MD98-953 954 2162. 955 Supplementary Table 3. Reconstructed stacks of SST, TWT, upper OHC and $\delta^{18}O_{sw}$, and simulated upper OHC, $\delta^{18}O_{sw}$ and $\delta^{18}O_{p}$. 956